Journal of Computational Physics 404 (2020) 109103

Contents lists available at ScienceDirect

Journal of Computational Physics

www.elsevier.com/locate/jcp

Backflow stabilization by deconvolution-based large eddy simulation modeling

Huijuan Xu [a,*], Davide Baroli [b], Francesca Di Massimo [c], Annalisa Quaini [d], Alessandro Veneziani [e,f]

[a] The George W. Woodruff School of Mechanical Engineering, Georgia Institute of Technology, Atlanta, GA, USA
[b] Aachen Institute for Advanced Study in Computational Engineering Science, Aachen, Germany
[c] Department of Mathematics, University of Pavia, Italy
[d] Department of Mathematics, University of Houston, Houston, TX, USA
[e] Department of Mathematics, Emory University, Atlanta, GA, USA
[f] Department of Computer Science, Emory University, Atlanta, GA, USA

ARTICLE INFO

Article history:
Received 3 June 2019
Received in revised form 2 November 2019
Accepted 5 November 2019
Available online 9 November 2019

Keywords:
Backflow instability
Large eddy simulation
Leray-α model
Computational hemodynamics

ABSTRACT

In the numerical simulations of incompressible fluids, the occurrence of incoming flows through outlet boundaries where Neumann conditions are prescribed may introduce the numerical instability known as the *backflow instability*. This backflow instability is related to the nonlinear convective term and is often challenging the numerical simulation of the blood flow in large vessels. In fact, the alternation of systole and diastole induces backflows at the outlets, which are usually Neumann boundaries since the lack of velocity data requires the prescription of traction/pressure conditions. The Reynolds numbers that trigger the backflow instability are generally moderate (in the range of a few hundreds and above).

In this work, we prove that a particular Large Eddy Simulation (LES) model implicitly stabilizes the backflow instability. This LES model uses deconvolution filters and is the basis of the so-called Evolve-Filter-Relax scheme recently introduced by Layton, Rebholz and their collaborators as an effective alternative to Direct Numerical Simulations for the moderate or large Reynolds number flow. With a judicious selection of the parameters of this LES scheme, it is possible to suppress the term that triggers the numerical backflow instability, so to obtain reliable and efficient numerical simulations. This is particularly attractive in computational clinical studies, where many cases need to be studied in a relatively short time.

We provide a rigorous proof of our statement and numerical evidence that corroborates the theory on both idealized and realistic cases. For the latter, we consider a patient-specific aortic aneurysm geometry. Aortic simulations feature Reynolds numbers and flow regimes that particularly benefit from this *serendipity* (aka 'two-birds-one-stone') circumstance, where a LES modeling is stabilizing a numerical artifact.

* Corresponding author at: The George W. Woodruff School of Mechanical Engineering, Georgia Institute of Technology, Atlanta, GA, USA.
E-mail address: huijuan.xu@gatech.edu (H. Xu).

https://doi.org/10.1016/j.jcp.2019.109103
0021-9991/

1. Introduction

Many challenges in modern computational fluid dynamics arise from the treatment of boundary conditions. This is particularly true in fields like computational hemodynamics, where the data needed to prescribe the boundary conditions are often incomplete or absent. It is practically impossible to prescribe Dirichlet velocity boundary conditions in hemodynamics as these data are mostly inaccessible in real (patient-specific) settings.

This circumstance gives rise to a series of numerical challenges like the *backflow instability*. This numerical trouble occurs when a fluid enters a Neumann outlet boundary. The convective term of the incompressible Navier-Stokes equations in presence of flow reversal is, in fact, responsible for an incoming energy that eventually triggers the numerical instability. This paper concerns the numerical stabilization of this problem via a Large Eddy Simulation (LES) modeling, in the context of simulating the blood flow in large vessels (aorta, in particular). Under realistic conditions, these cases suffer from the backflow instability but also may need a specific numerical treatment of the flow disturbances induced by physiopathological morphologies, like the one offered by the LES modeling. We show that the same LES model introduced to treat flow disturbances suppresses the backflow instability.

1.1. Problem background

Patient-specific computational hemodynamics provide detailed spatial and temporal information of the blood flow dynamics to facilitate the understanding of the disease progression for various aortic syndromes or the optimization of medical devices design. In the simulations, the three-dimensional Navier-Stokes equations are approximated in a truncated domain of the regions of interest reconstructed from patients' medical images. Boundary conditions at the truncated artificial boundaries describe the effect of the peripheral vascular system on the region of interest and therefore are of great importance to obtain the physiological solution [1–3]. As the patient-specific velocity fields at the exact boundaries are rarely available, Neumann boundary conditions are widely adopted with traction or pressure data that are often derived from 1D or 0D surrogate models leveraged by patients' data [4–8]. The circumstance that boundary data in computational hemodynamics are partially missing led to the concept of *defective boundary conditions*. In this frame, 1D and 0D model were often introduced to provide an educated estimate of missing data from measurements available in (accessible) vascular districts peripheral to the one of interest.

In aortic simulations, Neumann boundary conditions are commonly enforced at relative large branches, i.e. the supra-aortic branches, renal artery, common iliac arteries, etc. At these branches, reverse flows (aka backflows or inward flows) are present during late systole and early diastole, when the blood flow is decelerating. Due to the energy injection caused by the convection term at the Neumann boundaries, the backflow causes instability to the numerical solution even with moderate Reynolds numbers. There have been various studies on stabilizing the backflow instability with velocity-based, velocity gradient-based and other formulations [9–13]. Many of these contributions rely on the modification of the Neumann boundary conditions to damp flow reversal, following the ideas of [14], yet stemming from a different motivation.

Besides the backflow instability, the simulation of blood flow in the aorta is non-trivial due to the disturbed nature of the flow associated with a relatively large Reynolds number at the peak systole and a complex geometry induced by some pathologies [6,15,16]. The Direct Numerical Simulation of these flows would require a refinement level of the space reticulation able to capture the flow field at the smallest scale. The associated computational cost might be intimidatingly high, especially for time-sensitive clinical applications. Turbulence modeling has been adopted in simulating aortic flows in, e.g., [16,15]. Recently, a deconvolution-based LES model [17] has been shown to be able to capture the properties of disturbed flow using a coarse discretization mesh, thereby reducing the computational cost [6].

1.2. Aim of this work

In this work, we prove theoretically and demonstrate numerically that our deconvolution-based LES model implemented by the Evolve-Filter-Relax (EFR) scheme [17] is able to suppress the occurrence of the backflow instability with an appropriate selection of the model parameters. This means that not only it allows reliable numerical simulations even with relatively coarse meshes, as it properly includes the contribution of unresolved scales, but also automatically fixes the instability due to the flow reversal with a judicious calibration of the model parameters.

After recalling the basic features of our EFR-LES modeling, the rigorous proof of the backflow instability suppression by an energy analysis is given in Section 2. In Section 3, we test our statements on three data sets: the first is an idealized case in a cylinder inspired by a benchmark for backflow instability proposed recently [9]; the second is an idealized arch designed to trigger the numerical instability in order to test the parameter sensitivity; the last one is a patient-specific case of an abdominal aneurysm retrieved from the iCardioCloud Project [7]. Conclusions are drawn in Section 4.

1.3. Notation

In what follows, we refer to the usual notation $L^2(\Omega)$ for functions with square integrable according to Lebesgue. We do not introduce a different notation for scalar or vector functions as it will be clear from the context. Also, functions with s

distributional derivatives in $L^2(\Omega)$ will be denoted with the usual notation for Sobolev spaces $H^s(\Omega)$. As usual, $(\cdot,\cdot)$ denotes the scalar product in L^2 and $\|\cdot\|$ the associated norm.

In addition, we introduce the operators ∇^s and Δ^s, defined as

$$\nabla^s \mathbf{u} \equiv \frac{1}{2}(\nabla \mathbf{u} + \nabla \mathbf{u}^T), \qquad \Delta^s \mathbf{u} \equiv \nabla \cdot \left(\nabla^s \mathbf{u}\right) \tag{1}$$

where ∇^s is the symmetric part of the gradient.

2. Analysis of the backflow stabilization by the deconvolution-based LES model

2.1. The deconvolution-based LES model and the Evolve-Filter-Relax scheme

The motion of an incompressible, viscous fluid in a domain Ω over a time interval of interest $(0, T)$ is governed by the incompressible Navier-Stokes equations,

$$\rho \frac{\partial \mathbf{u}}{\partial t} + \rho(\mathbf{u}\cdot\nabla)\mathbf{u} - 2\mu\Delta^s\mathbf{u} + \nabla p = \mathbf{f}, \tag{2}$$

$$\nabla \cdot \mathbf{u} = 0 \tag{3}$$

with boundary conditions:

$$\mathbf{u} = \mathbf{u}_D \quad \text{on} \quad \Gamma_D \times (0,T)\,, \tag{4}$$

$$(2\mu\nabla^s\mathbf{u} - p\mathbf{I})\mathbf{n} = \mathbf{g}_N \quad \text{on} \quad \Gamma_N \times (0,T) \tag{5}$$

where $\mathbf{u}$ is the velocity, p is the pressure, ρ is the density, and μ is the dynamic viscosity. Here, Ω with boundary $\Gamma \equiv \Gamma_D \cup \Gamma_N$ ($\Gamma_D \cap \Gamma_N = \emptyset$) is a generic domain in 3D, T a final time, $\mathbf{u}_D$ and $\mathbf{g}_N$ are given data.

By a standard application of the incompressibility condition, it is promptly proved that

$$2\mu\Delta^s\mathbf{u} = \mu\nabla\cdot\left(\nabla\mathbf{u} + \nabla^T\mathbf{u}\right) = \mu\Delta\mathbf{u}$$

where Δ is the standard Laplace operator. As a matter of fact, usually the incompressible Navier-Stokes equations are written in this form. However, when we come to the variational formulation, the divergence operator is not applied to $\nabla^s\mathbf{u}$, so we are not allowed to cancel the transpose of the gradient operator. Nevertheless, the formulation with the regular Laplace is currently used in many contexts. The Laplace formulation has the advantage of an associated block-diagonal stiffness matrix, which is easier to store and solve. It has also been argued [1] that the regular form is more suitable for artificial boundary conditions, as it fixes some numerical troubles showing up with the correct symmetric formulation on a Neumann boundary. However, we prefer to stick with the original formulation (and the associated natural boundary conditions) based on the symmetric form, as this is generally appropriate in hemodynamics and fluid-structure interaction problems. It is worth noting that, from the analytical point of view in estimating the energy of the system, the regular form is technically easier, as it is associated directly with the regular H^1 norm $\|\mathbf{u}\|_{H^1} \equiv \left(\|\mathbf{u}\|^2_{L^2} + \|\nabla\mathbf{u}\|^2_{L^2}\right)^{1/2}$. However, note that the natural norm associated with the symmetric form $\|\mathbf{u}\|_s \equiv \left(\|\mathbf{u}\|^2_{L^2} + \|\nabla^s\mathbf{u}\|^2_{L^2}\right)^{1/2}$ is equivalent to the regular norm thanks to the Korn's inequality [18].

As well known, when the Reynolds number of the fluid increases past a certain threshold, the nonlinear convective term determines an energy cascade from large to small space scales. These dynamics challenge the numerical simulation, as the reticulation for the spatial discretization must adjust to properly describe the small-scale energy. The scale at which we can consider the energy to be dissipated is given by the Kolmogorov theory [19] as

$$\eta \approx \left(\frac{\mu^3 L}{\rho^3 U^3}\right)^{1/4} \approx LRe^{-3/4}$$

where L is a characteristic length of the problem, U the maximum velocity magnitude, and Re the Reynolds number. A possible approach to overcome the burden of exceedingly fine meshes is to resort to LES modeling. Generically speaking, LES incorporates the effect of small under-resolved space scales - i.e. in the range between η and the size of the mesh h (with $\eta < h$) - by an appropriate average-based approximation of their effect on the resolved scales. This general idea can be realized in different ways [20–23]. Here, we follow an approach developed by W. Layton, L. Rebholz and collaborators [24–27], where the unresolved scales are incorporated into the simulation by a differential operator acting as a filter, triggered by an appropriate indicator function that identifies where and when we actually have unresolved scales.

We refer to a specific formulation of this filtering approach advocated in [28] and successively considered in [17]. The model reads:

$$\rho\frac{\partial \mathbf{u}}{\partial t}+\rho\left(\mathbf{u}_f\cdot\nabla\right)\mathbf{u}-2\mu\Delta^s\mathbf{u}+\nabla p=\mathbf{f}, \tag{6}$$

$$\nabla\cdot\mathbf{u}=0, \tag{7}$$

$$-2\delta^2\nabla\cdot\left(a(\mathbf{u})\nabla^s\mathbf{u}_f\right)+\mathbf{u}_f+\nabla p_f=\mathbf{u}, \tag{8}$$

$$\nabla\cdot\mathbf{u}_f=0; \tag{9}$$

in $\Omega\times(0,T)$. The equations (8)-(9) represent the nonlinear filter applied to $\mathbf{u}$. Here, $\mathbf{u}_f$ is the *filtered velocity*, δ can be interpreted as the *filtering radius* (a parameter related to the mesh size h), p_f is a Lagrange multiplier to enforce the incompressibility constraint for $\mathbf{u}_f$, and $a(\cdot)$ is a scalar function called *indicator function*. Problem (6)-(9) is endowed with the boundary conditions

$$\mathbf{u}=\mathbf{u}_f=\mathbf{u}_D \quad \text{on} \quad \Gamma_D\times(0,T), \tag{10}$$

$$(2\mu\nabla^s\mathbf{u}-p\mathbf{I})\mathbf{n}=\mathbf{g}_N \quad \text{on} \quad \Gamma_N\times(0,T), \tag{11}$$

$$(2\delta^2 a(\mathbf{u})\nabla^s\mathbf{u}_f-p_f\mathbf{I})\mathbf{n}=\mathbf{0} \quad \text{on} \quad \Gamma_N\times(0,T). \tag{12}$$

The role of the indicator function is to detect the regions of disturbed flow. Below we present our choice for $a(\cdot)$, which is crucial for the success of the Leray model. We choose a deconvolution-based indicator function:

$$a(\mathbf{u})\equiv|\mathbf{u}-D(F(\mathbf{u}))|,$$

where F denotes the linear Helmholtz operator

$$F\equiv(I-\delta^2\Delta)^{-1}$$

and D is its approximate inverse obtained by a truncation of the Neumann expansion of $I-(I-F)=\sum_{k=0}^{\infty}(I-F)^k$ [28,17]. This approach goes under the name of *Van Cittert-Helmholtz deconvolution filter*.

For the numerical approximation, system (6)-(9) requires time and space discretizations. The time discretization can be carried out by a collocation finite-difference approach. To this aim, we introduce a time step Δt (uniform, for simplicity) and locate the problem in the instants $t^j\equiv j\Delta t$, for $j=1,\ldots,N_T$, where $T=N_T\Delta t$. The time-derivative is then approximated by finite differences involving the unknowns in these collocation points. We adopt a Backward Differentiation Formula of order p (BDFp), see e.g. [29]. The Leray system discretized in time reads: given $\mathbf{u}^0$, for $n\geq 0$ find the solution $(\mathbf{u}^{n+1},p^{n+1},\mathbf{u}_f^{n+1},p_f^{n+1})$ of the system:

$$\rho\frac{\alpha}{\Delta t}\mathbf{u}^{n+1}+\rho(\mathbf{u}_f^{n+1}\cdot\nabla)\mathbf{u}^{n+1}-2\mu\Delta^s\mathbf{u}^{n+1}+\nabla p^{n+1}=\mathbf{b}^{n+1}, \tag{13}$$

$$\nabla\cdot\mathbf{u}^{n+1}=0, \tag{14}$$

$$-2\delta^2\nabla\cdot\left(a(\mathbf{u}^{n+1})\nabla^s\mathbf{u}_f^{n+1}\right)+\mathbf{u}_f^{n+1}+\nabla p_f^{n+1}=\mathbf{u}^{n+1}, \tag{15}$$

$$\nabla\cdot\mathbf{u}_f^{n+1}=0, \tag{16}$$

where α is a coefficient that depends on the order of BDF chosen, and $\mathbf{b}^{n+1}$ contains the forcing term $\mathbf{f}^{n+1}$ and the solution at the previous time steps used to approximate the time derivative of $\mathbf{u}$ at time t^{n+1}. For example,

$$\text{BDF1}:\begin{cases}\partial_t\mathbf{u}\simeq\dfrac{1}{\Delta t}\left(\mathbf{u}^{n+1}-\mathbf{u}^n\right)\\ \alpha=1\\ \mathbf{b}^{n+1}=\mathbf{f}^{n+1}+\dfrac{1}{\Delta t}\mathbf{u}^n\end{cases},\quad \text{BDF2}:\begin{cases}\partial_t\mathbf{u}\simeq\dfrac{1}{2\Delta t}\left(3\mathbf{u}^{n+1}-4\mathbf{u}^n+\mathbf{u}^{n-1}\right)\\ \alpha=3/2\\ \mathbf{b}^{n+1}=\mathbf{f}^{n+1}+\dfrac{1}{2\Delta t}\left(4\mathbf{u}^n-\mathbf{u}^{n-1}\right)\end{cases}. \tag{17}$$

The semi-discretized system (13)-(16) can be efficiently implemented in the so-called *Evolve-Filter-Relax* scheme. Set

$$\mu_f^{n+1}(\mathbf{v}^{n+1})\equiv\rho\frac{\delta^2}{\Delta t}a(\mathbf{v}^{n+1}), \tag{18}$$

$$L_{NS}[\mathbf{u}^*]\mathbf{v}^{n+1}\equiv\rho\left(\mathbf{u}^*\cdot\nabla\right)\mathbf{v}^{n+1}-2\mu\Delta^s\mathbf{v}^{n+1}, \tag{19}$$

$$L_F[\mathbf{v}^{n+1}]\mathbf{v}_f^{n+1}\equiv-\nabla\cdot\left[2\mu_f^{n+1}(\mathbf{v}^{n+1})\nabla^s\mathbf{v}_f^{n+1}\right]. \tag{20}$$

Note that, for easiness of notation, the dependence of μ_f on $\mathbf{v}^{n+1}$ will be understood, as it is unambiguous in the context.

The EFR algorithm reads as follows: given the velocities $\mathbf{u}^k$ $(k=n-p+1,\ldots,n)$ needed for the approximation of $\partial_t\mathbf{u}$ by BDFp at t^{n+1},

i) *Evolve: find intermediate velocity and pressure* $(\mathbf{v}^{n+1}, q^{n+1})$*, such that*

$$\rho\frac{\alpha}{\Delta t}\mathbf{v}^{n+1} + L_{NS}[\mathbf{u}^*]\mathbf{v}^{n+1} + \nabla q^{n+1} = \mathbf{b}^{n+1}, \tag{21}$$

$$\nabla\cdot\mathbf{v}^{n+1} = 0, \tag{22}$$

with boundary conditions

$$\mathbf{v}^{n+1} = \mathbf{u}_D^{n+1} \quad \text{on} \quad \Gamma_D, \tag{23}$$

$$(2\mu\nabla^s\mathbf{v}^{n+1} - q^{n+1}\mathbf{I})\mathbf{n} = \mathbf{g}_N^{n+1} \quad \text{on} \quad \Gamma_N. \tag{24}$$

In eq. (21), $\mathbf{u}^*$ is a suitable approximation of the end-of-step velocity $\mathbf{u}^{n+1}$ based on previous time-steps solutions.

ii) *Filter: find* $(\mathbf{v}_f^{n+1}, q_f^{n+1})$*, such that*

$$\frac{\rho}{\Delta t}\mathbf{v}_f^{n+1} + L_F[\mathbf{v}^{n+1}]\mathbf{v}_f^{n+1} + \nabla q_f^{n+1} = \frac{\rho}{\Delta t}\mathbf{v}^{n+1}, \tag{25}$$

$$\nabla\cdot\mathbf{v}_f^{n+1} = 0, \tag{26}$$

with boundary conditions

$$\mathbf{v}_f^{n+1} = \mathbf{u}_D^{n+1} \quad \text{on} \quad \Gamma_D, \tag{27}$$

$$(2\mu_f^{n+1}\nabla^s\mathbf{v}_f^{n+1} - q_f^{n+1}\mathbf{I})\mathbf{n} = \mathbf{0} \quad \text{on} \quad \Gamma_N. \tag{28}$$

iii) *Relax: set*

$$\mathbf{u}^{n+1} = (1-\chi)\mathbf{v}^{n+1} + \chi\mathbf{v}_f^{n+1}, \tag{29}$$

$$p^{n+1} = q^{n+1} + \alpha\chi q_f^{n+1}, \tag{30}$$

where $\chi \in [0,1]$ is a relaxation parameter.

This implementation of the Van Cittert-Helmholtz deconvolution filter has been analyzed in [17]. Strictly speaking, eq. (30) is not a relaxation, but it stems form the formulation of the Evolve-Filter-Relax method. A classical relaxation step is possible too. However, in [17] we demonstrated that eq. (30) leads to superior numerical results, so we stick to it.

2.2. The root of the backflow instability

The occurrence of the backflow instability can be explained by looking at the energy estimate for the Navier-Stokes equations (2), (3). For the stability analysis, let us assume that all the Dirichlet and Neumann data as well as the forcing term are set to 0 so to consider the decay of the solution from a generic initial condition $\mathbf{u}_0$. Following standard arguments, we multiply the momentum equation by the velocity $\mathbf{u}$ and the mass conservation by the pressure field p, we integrate on the space time domain $\Omega\times(0,T]$. Let us denote for the sake of brevity

$$E(T) \equiv \frac{\rho}{2}\|\mathbf{u}\|_{L^2}^2(T) + \mu\int_0^T \|\nabla^s\mathbf{u}\|_{L^2}^2(t)dt.$$

With a standard procedure, we get

$$E(T) + \frac{1}{2}\int_0^T\int_{\Gamma_N} |\mathbf{u}|^2\mathbf{u}\cdot\mathbf{n}d\gamma dt \le \|\mathbf{u}_0\|_{L^2}^2 \equiv E(0).$$

Here, $\mathbf{n}$ is the outward normal unit vector. If $\mathbf{u}\cdot\mathbf{n}\ge 0$ for any $t>0$, then the previous inequality does actually provide a stability estimate for the solution, as clearly we can conclude that $\|\mathbf{u}\|_{L^2}^2(T) \le \|\mathbf{u}_0\|_{L^2}^2$ for any $T>0$. This fails in the case of backflows, as *a priori* we may loose the control on the sign of $\int_0^T\int_{\Gamma_N}|\mathbf{u}|^2\mathbf{u}\cdot\mathbf{n}d\gamma dt$ and eventually on the bound for $E(T)$.

To fix this numerical problem grounded in the occurrence of physical flow reversal on Neumann boundaries, several remedies have been proposed, ranging from the introduction of flow extensions, or specific regions at the boundaries to damp the incoming energy [10], to the constraint of favorable velocity profiles by Lagrange multipliers [30], to the introduction of specific stabilization of the tangential components of the stress tensor [11,12]. Benchmarks and comparisons among the different strategies have been considered in [9,13].

A popular stabilization technique relies on the modification of the Neumann condition into a Robin one, with a resistance parameter R. This can be done in several ways [14,31]. We specifically mention the excellent description in [10,9]. For instance, in a simplified setting, in the strong form we can prescribe on $\Gamma_N \times (0, T)$

$$\left((\mu \nabla^s \mathbf{u} - \left(p - R \int_{\Gamma_N} \mathbf{u} \cdot \mathbf{n} d\gamma \right) \mathbf{I} \right) \mathbf{n} = g_N \mathbf{n}, \tag{31}$$

corresponding to the introduction of a pressure drop in the direction of the flow weighted by the coefficient R. Specifically, with this term, the energy estimate (for $g_N = 0$) becomes

$$E(T) + \frac{1}{2} \int_0^T \int_{\Gamma_N} |\mathbf{u}|^2 \mathbf{u} \cdot \mathbf{n} d\gamma dt + R \int_0^T \left(\int_{\Gamma_N} \mathbf{u} \cdot \mathbf{n} d\gamma \right)^2 dt \leq \|\mathbf{u}_0\|_{L^2}^2 \equiv E(0).$$

For a judicious calibration of the parameter R, the sum of the second and third terms on the left hand side is positive, to obtain the desired bound. This modifies the prescribed boundary conditions, with a damping as a sort lumped parameter modeling of a flow extension [4].

In the subsequent section, we prove that with EFR-LES modeling there is no need of acting on the boundary conditions to obtain the bound on the discrete counterpart of $E(T)$ and eventually on the numerical solution.

2.3. Main result

To establish the theoretical result showing that the numerical solution of our EFR-LES scheme is bounded by the data for a judicious choice of the parameters δ and χ, we postulate some regularity for the domain and the data, to assume $\mathbf{u} \in H^3(\Omega)$. For simplicity, we refer our analysis to the regular Laplace operator as opposed to the symmetric one Δ^s, the extension to this case being a matter of technicalities. Also, we refer to the time discretization BDF1 (Implicit Euler) scheme, as this is an unconditionally stable method, with no limitations on the time step to achieve stability. We argue (and demonstrate numerically) that the analysis can be extended to high order time discretizations, with the possible limitations on the time step required by the time advancing method.

Theorem. *Assume that the data of the problem at hand are regular enough s.t.* $\mathbf{u} \in L^2(0, T, H^3(\Omega))$. *Also, assume that the problem has homogeneous boundary conditions (*$\mathbf{u}_D = 0$ *on* Γ_D *and* $g_N = 0$ *on* Γ_N*) and a null forcing term* $\mathbf{f}$. *For* $\chi \to 1^-$ *and a suitable choice of the filter radius* δ, *the EFR-LES scheme features a solution such that for any* $n > 0$

$$\|\mathbf{u}^n\|_{L^2} \leq \|\mathbf{u}_0\|_{L^2}. \tag{32}$$

The condition (32) actually means that the backflow instability cannot occur, as we will demonstrate numerically.

Proof. We restart from the reinterpretation of the method as a perturbation of the Navier-Stokes equations (see [17]), with BDF1 time discretization ($\alpha = 1$), homogeneous boundary data and $\mathbf{f} = \mathbf{0}$:

$$\frac{\rho}{\Delta t} \mathbf{u}^{n+1} + L_{NS}[\mathbf{u}^*]\mathbf{u}^{n+1} + \nabla(q^{n+1} + \chi q_f^{n+1}) + \chi \{ L_{NS}[\mathbf{u}^*] \left(\mathbf{v}^{n+1} - \mathbf{v}_f^{n+1} \right) + \alpha L_F[\mathbf{v}^{n+1}]\mathbf{v}_f^{n+1} \} = \frac{\rho}{\Delta t} \mathbf{u}^n, \tag{33}$$

where the right hand side incorporates the terms of the discretization of the time derivative. The third term on the first line can be written as ∇p^{n+1}, using (30).

In what follows, we use the following well-known generic identities for two generic arguments of the scalar product a and b

$$(a, a-b) = \frac{1}{2}\|a\|^2 + \frac{1}{2}\|a-b\|^2 - \frac{1}{2}\|b\|^2, \qquad (b, a-b) = \frac{1}{2}\|a\|^2 - \frac{1}{2}\|a-b\|^2 - \frac{1}{2}\|b\|^2 \tag{34}$$

and the specific equations

$$\mathbf{v}^{n+1} - \mathbf{u}^{n+1} = \chi \left(\mathbf{v}^{n+1} - \mathbf{v}_f^{n+1} \right), \quad \chi \mathbf{v}_f^{n+1} = \mathbf{u}^{n+1} - (1-\chi)\mathbf{v}^{n+1}. \tag{35}$$

Also, we will refer to the traditional form of the gradient for simplicity.

By standard multiplication of (33) by $\mathbf{u}^{n+1}$ and integration by parts, considering the Neumann conditions for $\mathbf{v}^{n+1}$ and $\mathbf{v}_f^{n+1}$ on Γ_N we obtain

$$\frac{\rho}{\Delta t}\|\mathbf{u}^{n+1}\|^2+\frac{1}{2}\int_{\Gamma_N}\rho|\mathbf{u}^{n+1}|^2\mathbf{u}^*\cdot\mathbf{n}d\gamma+\mu\|\nabla\mathbf{u}^{n+1}\|^2+$$
$$\chi\left(\int_\Omega\rho(\mathbf{u}^*\cdot\nabla)(\mathbf{v}^{n+1}-\mathbf{v}_f^{n+1})\cdot\mathbf{u}^{n+1}d\omega+\mu(\nabla(\mathbf{v}^{n+1}-\mathbf{v}_f^{n+1}),\nabla\mathbf{u}^{n+1})\right)+ \tag{36}$$
$$\chi(\mu_f\nabla\mathbf{v}_f^{n+1},\nabla\mathbf{u}^{n+1})=\frac{\rho}{\Delta t}(\mathbf{u}^n,\mathbf{u}^{n+1}).$$

As previously pointed out, the second term in the first line in the presence of backflow prevents a bound on the solution, as it may be negative. To the two terms in the second line we apply the first equation in (35) and obtain

$$\int_\Omega\rho(\mathbf{u}^*\cdot\nabla)(\mathbf{v}^{n+1}-\mathbf{u}^{n+1})\cdot\mathbf{u}^{n+1}d\omega+\mu(\nabla(\mathbf{v}^{n+1}-\mathbf{u}^{n+1}),\nabla\mathbf{u}^{n+1})$$
$$=\int_\Omega\rho(\mathbf{u}^*\cdot\nabla)(\mathbf{v}^{n+1}-\mathbf{u}^{n+1})\cdot\mathbf{u}^{n+1}d\omega+\frac{\mu}{2}\|\nabla\mathbf{v}^{n+1}\|^2-\frac{\mu}{2}\|\nabla(\mathbf{v}^{n+1}-\mathbf{u}^{n+1})\|^2-\frac{\mu}{2}\|\nabla\mathbf{u}^{n+1}\|^2, \tag{37}$$

where we used the second identity in (34).

For the term in the third line of (36), using the second equation in (35) we obtain

$$(\mu_f\nabla\mathbf{u}^{n+1},\nabla\mathbf{u}^{n+1})-(1-\chi)(\mu_f\nabla\mathbf{v}^{n+1},\nabla\mathbf{u}^{n+1}). \tag{38}$$

From (36), after a standard application of the Young inequality at the right hand side, we obtain therefore

$$\frac{\rho}{2\Delta t}\|\mathbf{u}^{n+1}\|^2+\frac{1}{2}\int_{\Gamma_N}\rho|\mathbf{u}^{n+1}|^2\mathbf{u}^*\cdot\mathbf{n}d\gamma+\frac{\mu}{2}\|\nabla\mathbf{u}^{n+1}\|^2+\frac{\mu}{2}\|\nabla\mathbf{v}^{n+1}\|^2-\frac{\mu}{2}\|\nabla(\mathbf{v}^{n+1}-\mathbf{u}^{n+1})\|^2+$$
$$\rho\int_\Omega(\mathbf{u}^*\cdot\nabla)(\mathbf{v}^{n+1}-\mathbf{u}^{n+1})\cdot\mathbf{u}^{n+1}d\omega+ \tag{39}$$
$$(\mu_f\nabla\mathbf{u}^{n+1},\nabla\mathbf{u}^{n+1})-(1-\chi)(\mu_f\nabla\mathbf{v}^{n+1},\nabla\mathbf{u}^{n+1})\le\frac{\rho}{2\Delta t}\|\mathbf{u}^n\|^2.$$

Let us focus on the term in the second line. By direct computation and the divergence Theorem, we have

$$\int_\Omega(\mathbf{u}^*\cdot\nabla)(\mathbf{v}^{n+1}-\mathbf{u}^{n+1})\cdot\mathbf{u}^{n+1}d\omega=\frac{1}{2}\int_\Omega(\mathbf{u}^*\cdot\nabla)\mathbf{v}^{n+1}\cdot\mathbf{u}^{n+1}d\omega-\frac{1}{2}\int_\Omega(\mathbf{u}^*\cdot\nabla)\mathbf{u}^{n+1}\cdot\mathbf{u}^{n+1}d\omega+$$
$$\frac{1}{2}\int_\Omega(\mathbf{u}^*\cdot\nabla)(\mathbf{v}^{n+1}-\mathbf{u}^{n+1})\cdot(\mathbf{u}^{n+1}-\mathbf{v}^{n+1})d\omega+\frac{1}{2}\int_\Omega(\mathbf{u}^*\cdot\nabla)\mathbf{v}^{n+1}\cdot\mathbf{v}^{n+1}d\omega=$$
$$\frac{1}{2}\int_{\Gamma_N}(\mathbf{u}^*\cdot\mathbf{n})\mathbf{v}^{n+1}\cdot\mathbf{u}^{n+1}d\gamma-\frac{1}{2}\int_\Omega(\mathbf{u}^*\cdot\nabla)\mathbf{u}^{n+1}\cdot\mathbf{v}^{n+1}d\omega$$
$$-\frac{1}{4}\int_{\Gamma_N}(\mathbf{u}^*\cdot\mathbf{n})|\mathbf{u}^{n+1}|^2d\gamma-\frac{1}{4}\int_{\Gamma_N}(\mathbf{u}^*\cdot\mathbf{n})|\mathbf{v}^{n+1}-\mathbf{u}^{n+1}|^2d\gamma+\frac{1}{4}\int_{\Gamma_N}(\mathbf{u}^*\cdot\mathbf{n})|\mathbf{v}^{n+1}|^2d\gamma$$
$$-\frac{1}{2}\int_\Omega(\mathbf{u}^*\cdot\nabla)\mathbf{u}^{n+1}\cdot\mathbf{v}^{n+1}d\omega$$

Sum the term $\frac{1}{2}\int_{\Gamma_N}|\mathbf{u}^{n+1}|^2\mathbf{u}^*\cdot\mathbf{n}d\gamma$ in (39) to what we obtained above, to get

$$\frac{1}{2}\int_{\Gamma_N}(\mathbf{u}^*\cdot\mathbf{n})\mathbf{v}^{n+1}\cdot\mathbf{u}^{n+1}d\gamma-\int_\Omega(\mathbf{u}^*\cdot\nabla)\mathbf{u}^{n+1}\cdot\mathbf{v}^{n+1}d\omega$$
$$+\frac{1}{4}\int_{\Gamma_N}(\mathbf{u}^*\cdot\mathbf{n})|\mathbf{u}^{n+1}|^2d\gamma-\frac{1}{4}\int_{\Gamma_N}(\mathbf{u}^*\cdot\mathbf{n})|\mathbf{v}^{n+1}-\mathbf{u}^{n+1}|^2d\gamma+\frac{1}{4}\int_{\Gamma_N}(\mathbf{u}^*\cdot\mathbf{n})|\mathbf{v}^{n+1}|^2d\gamma=$$
$$-\int_\Omega(\mathbf{u}^*\cdot\nabla)\mathbf{u}^{n+1}\cdot\mathbf{v}^{n+1}d\omega+\frac{1}{4}\int_{\Gamma_N}(\mathbf{u}^*\cdot\mathbf{n})\left(|\mathbf{u}^{n+1}|^2+|\mathbf{v}^{n+1}|^2-2\mathbf{v}^{n+1}\cdot\mathbf{u}^{n+1}\right)d\gamma$$

$$-\frac{1}{4}\int_{\Gamma_N}\left(\mathbf{u}^*\cdot\mathbf{n}\right)|\mathbf{v}^{n+1}-\mathbf{u}^{n+1}|^2 d\gamma=-\int_{\Omega}(\mathbf{u}^*\cdot\nabla)\mathbf{u}^{n+1}\cdot\mathbf{v}^{n+1}d\omega.$$

Now, let us consider the second term in the third line of (39). Using the fact that

$$\mathbf{u}^{n+1}=\mathbf{v}^{n+1}-\chi(\mathbf{v}^{n+1}-\mathbf{v}_f^{n+1})$$

we obtain

$$\begin{aligned}&-(1-\chi)(\mu_f\nabla\mathbf{v}^{n+1},\nabla\mathbf{u}^{n+1})=(1-\chi)\left[-(\mu_f\nabla\mathbf{v}^{n+1},\nabla\mathbf{v}^{n+1})\right.\\&\left.+\chi(\mu_f\nabla\mathbf{v}^{n+1},\nabla(\mathbf{v}^{n+1}-\mathbf{v}_f^{n+1}))\right]=(1-\chi)\left[-\left(1-\frac{\chi}{2}\right)(\mu_f\nabla\mathbf{v}^{n+1},\nabla\mathbf{v}^{n+1})\right.\\&\left.+\frac{\chi}{2}(\mu_f\nabla(\mathbf{v}^{n+1}-\mathbf{v}_f^{n+1}),\nabla(\mathbf{v}^{n+1}-\mathbf{v}_f^{n+1}))-\frac{\chi}{2}(\mu_f\nabla\mathbf{v}_f^{n+1},\nabla\mathbf{v}_f^{n+1})\right].\end{aligned}$$

Finally, notice that

$$\frac{\mu}{2}\|\nabla\mathbf{u}^{n+1}\|^2+\frac{\mu}{2}\|\nabla\mathbf{v}^{n+1}\|^2-\frac{\mu}{2}\|\nabla(\mathbf{v}^{n+1}-\mathbf{u}^{n+1})\|^2=\mu(\nabla\mathbf{u}^{n+1},\nabla\mathbf{v}^{n+1}).$$

Collecting all the steps so far, inequality (39) becomes

$$\begin{aligned}&\frac{\rho}{2\Delta t}\|\mathbf{u}^{n+1}\|^2-\rho\int_{\Omega}(\mathbf{u}^*\cdot\nabla)\mathbf{u}^{n+1}\cdot\mathbf{v}^{n+1}d\omega+\mu(\nabla\mathbf{u}^{n+1},\nabla\mathbf{v}^{n+1})+(\mu_f\nabla\mathbf{u}^{n+1},\nabla\mathbf{u}^{n+1})\\&+(1-\chi)\left[-\left(1-\frac{\chi}{2}\right)(\mu_f\nabla\mathbf{v}^{n+1},\nabla\mathbf{v}^{n+1})+\frac{\chi}{2}(\mu_f\nabla(\mathbf{v}^{n+1}-\mathbf{v}_f^{n+1}),\nabla(\mathbf{v}^{n+1}-\mathbf{v}_f^{n+1}))\right.\\&\left.-\frac{\chi}{2}(\mu_f\nabla\mathbf{v}_f^{n+1},\nabla\mathbf{v}_f^{n+1})\right]\le\frac{\rho}{2\Delta t}\|\mathbf{u}^n\|^2.\end{aligned}\tag{40}$$

Notice that for $\chi=0$, i.e. in absence of stabilization ($\mathbf{u}^{n+1}=\mathbf{v}^{n+1}$), we retrieve the standard energy estimate where the convective term is negative for the backflows, so it prevents a bound on the solution. Also, notice that all the terms multiplied by $(1-\chi)$ are negative. This can be promptly proved under the assumption that $\mathbf{v}^{n+1}\in H^3(\Omega)$ (which is a consequence of regularity of the data as inferred in [32]). In this case, also $\mathbf{v}_f^{n+1}\in H^3(\Omega)$. Then, from the weak formulation of (25), with the test function $\nabla\cdot(\mu_f\nabla\mathbf{v}_f^{n+1})$ (that belongs to H^1 for the regularity assumptions), we find that $(\mu_f\nabla\mathbf{v}^{n+1},\nabla\mathbf{v}_f^{n+1})>0$ [33–36]. The statement follows observing that

$$\begin{aligned}&-(1-\chi)\left(1-\frac{\chi}{2}\right)(\mu_f\nabla\mathbf{v}^{n+1},\nabla\mathbf{v}^{n+1})+\frac{\chi}{2}(1-\chi)(\mu_f\nabla(\mathbf{v}^{n+1}-\mathbf{v}_f^{n+1}),\nabla(\mathbf{v}^{n+1}-\mathbf{v}_f^{n+1}))\\&-\frac{\chi}{2}(1-\chi)(\mu_f\nabla\mathbf{v}_f^{n+1},\nabla\mathbf{v}_f^{n+1})=-(1-\chi)^2(\mu_f\nabla\mathbf{v}^{n+1},\nabla\mathbf{v}^{n+1})-(1-\chi)\chi(\mu_f\nabla\mathbf{v}^{n+1},\nabla\mathbf{v}_f^{n+1}).\end{aligned}$$

Another way of proving the statement is to recall that all the terms multiplied by $(1-\chi)$ come from the second term in the third line of (39). Then, by using (29), we have:

$$-(1-\chi)(\mu_f\nabla\mathbf{v}^{n+1},\nabla\mathbf{u}^{n+1})=-(1-\chi)^2(\mu_f\nabla\mathbf{v}^{n+1},\nabla\mathbf{v}^{n+1})-(1-\chi)\chi(\mu_f\nabla\mathbf{v}^{n+1},\nabla\mathbf{v}_f^{n+1}).$$

Now, we prove that for $\chi=1$ the stabilizing term, i.e. the fourth term in (40), can be selected to control the convective term. In fact, for $\chi=1$, we have $\mathbf{u}^{n+1}=\mathbf{v}_f^{n+1}$. Thus, following the same arguments used above and noting that $\mu_f\ge c>0$ for c constant we have that $(\nabla\mathbf{v}^{n+1},\nabla\mathbf{u}^{n+1})>0$. Then, (40) reads

$$\frac{\rho}{2\Delta t}\|\mathbf{u}^{n+1}\|^2-\int_{\Omega}\rho(\mathbf{u}^*\cdot\nabla)\mathbf{u}^{n+1}\cdot\mathbf{v}^{n+1}d\omega+\mu(\nabla\mathbf{u}^{n+1},\nabla\mathbf{v}^{n+1})+\alpha(\mu_f\nabla\mathbf{u}^{n+1},\nabla\mathbf{u}^{n+1})\le\frac{\rho}{2\Delta t}\|\mathbf{u}^n\|^2.\tag{41}$$

As μ_f is proportional to the filter radius δ^2, it is enough to select a radius large enough to guarantee

$$(\mu_f\nabla\mathbf{u}^{n+1},\nabla\mathbf{u}^{n+1})\ge\left|\int_{\Omega}\rho(\mathbf{u}^*\cdot\nabla)\mathbf{u}^{n+1}\cdot\mathbf{v}^{n+1}d\omega\right|$$

As the entire energy depends continuously on χ, by a continuity argument we have that for $\chi\to1^-$

$$\|\mathbf{u}^{n+1}\|\le\|\mathbf{u}^n\|$$

and then recursively

$$\|\mathbf{u}^n\|\le\|\mathbf{u}_0\|.\quad\square$$

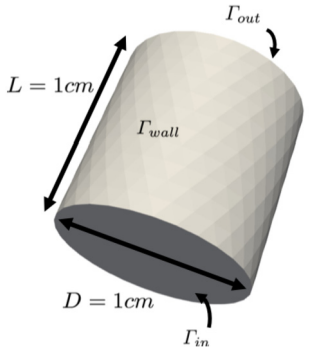

Fig. 1. Test 1: asymmetrical reversed flow in a straight channel.

Although the proof does not give a specific indication on the choice of δ, it does actually show that there exists a choice of the filtering radius and the relaxation parameter that allows to control the occurrence of backflows. This statement is supported by the numerical experiments in the next Section. Based on the results presented here, we will draw some practical guidelines on the selection of the parameters in Section 4.

3. Numerical experiments

In order to verify our theory numerically, we perform three tests. The first two tests feature idealized geometries: a straight channel for test 1 and a curved channel for test 2. For the third test, we use a patient-specific geometry of the aorta with an abdominal aneurysm. In all the tests, a combination of the geometry and boundary conditions trigger the backflow instability. The purpose of Test 1 is to compare the results obtained using our EFR-LES model with the benchmark results in [9] for a "stress test" that does not refer to any specific physical condition. Test 2 is not realistic either, yet it aims at investigating the sensitivity of the stabilization provided by the EFR-LES model to model parameters δ and χ for different meshes and time steps. Finally, test 3 assesses the efficacy of our method in a realistic setting. The results are compared with an alternative methodology currently used in the literature, emphasizing the excellent accuracy in terms of flow rates.

We use the EFR-LES scheme (21)-(30), with a space discretization based on inf-sup stable finite element pairs: $\mathbb{P}_2/\mathbb{P}_1$ for test 1 and 2, and $\mathbb{P}_1-\text{Bubble}/\mathbb{P}_1$ for test 3. Since test 3 involves flow in a complex geometry, the choice of the $\mathbb{P}_1-\text{Bubble}/\mathbb{P}_1$ pair is motivated by the reduced computational cost. For all the tests we used BDF2 (17) for the time-discretization of problem (21)-(22), with a semi-implicit treatment of the convective term based on a second order extrapolation.

The numerical simulations for test 1 and 3 were performed with finite element library `LifeV` [37,38], while we used `FreeFem++` [39] for test 2.

3.1. Test 1: asymmetrical reversed flow in a straight channel

Inspired by a benchmark test proposed in [9] for a 2D problem with backflow in a rectangular domain, we consider fluid flow in a 3D straight channel with the inflow boundary condition given by a skewed Womersley-like solution. We recall that the Womersley solution is the counterpart of the well-known Poiseuille-Hagen solution for a steady incompressible fluid in a cylinder when a periodic-in-time pressure drop is prescribed [40]. The 2D version of the Womersley solution advocated in [9] can be found in [41].

3.1.1. Problem setup

Let $\mathbf{x} = (x_1, x_2, x_3)$ be a point in $\mathbb{R}^3$. The domain $\Omega \subset \mathbb{R}^3$ is a cylinder, shown in Fig. 1, with $\Gamma_{in} = \{\mathbf{x} \in \Omega : x_3 = 0\}$, $\Gamma_{out} = \{\mathbf{x} \in \Omega : x_3 = L\}$, and $\Gamma_{wall} = \{\mathbf{x} \in \Omega : \sqrt{x_1^2 + x_2^2} = D/2\}$. Here, L and D are the cylinder height and diameter, respectively. For the numerical results in Sec. 3.1.2, we set $D = L = 1$ cm. We consider the flow of an incompressible fluid with density $\rho = 1.06$ g/cm^3 and viscosity $\mu = 0.035$ dyn s/cm^2 (these are typical values for blood flow problems) in domain Ω.

Let W be a Womersley-like velocity profile based on the 2D Womersley solution:

$$W(\mathbf{x}, t) = \sum_{k=0}^{K} d_k \Phi_k(t) S_k(\mathbf{x})$$

with

$$d_k = \frac{4\Delta P}{\rho\pi(2k+1)((2k+1)^4\sigma^2\pi^4 + \omega^2)}, \quad \sigma = \frac{\mu}{\rho L^2},$$

$$\Phi_k(t) = (2k+1)^2\sigma\pi^2\sin(\omega t) - \omega\cos(\omega t) + \omega\exp((-2k+1)^2\sigma\pi),$$

$$S_k(\mathbf{x}) = \sin\left(\pi(2k+1)\frac{\sqrt{(x_1^2+x_2^2)}}{D}\right).$$

Here, K is the number of modes, ΔP and ω are the prescribed pressure drop and its frequency. For the numerical results in Sec. 3.1.2, we set $K = 19$, $\Delta P = 40$ dyn/cm^2, and $\omega = 2\pi$ rad/s.

We define velocity $\mathbf{u}_W$ as a skewed velocity profile based on W [9]:

$$\mathbf{u}_W = \left(0, 0, \frac{3}{2}x_1^{0.7}W(\mathbf{x}, t)\right)$$

where the x_1 factor is intended to break the symmetry so to trigger the non-linear convective terms, which are otherwise vanishing in the original Womersley solution. Then, we call reference solution $(\mathbf{u}_{ref}, p_{ref})$ the solution to the Navier-Stokes equations (2)-(3) with boundary conditions:

$$\mathbf{u}_{ref} = \mathbf{u}_W \quad \text{on} \quad \Gamma_{in}\times(0,T), \tag{42}$$

$$\mathbf{u}_{ref} = \mathbf{0} \quad \text{on} \quad \Gamma_{wall}\times(0,T), \tag{43}$$

$$(\mu\nabla\mathbf{u}_{ref} - p_{ref}\mathbf{I})\mathbf{n} = \mathbf{0} \quad \text{on} \quad \Gamma_{out}\times(0,T). \tag{44}$$

The Navier-Stokes problem with these boundary conditions (42)-(44) will be denoted hereafter as *reference problem*.

To induce backflow instability and therefore test the performance of the EFR scheme, this first benchmark problem is constructed with Neumann boundary condition at Γ_{in} corresponding to the reference solution $(\mathbf{u}_{ref}, p_{ref})$. In particular, let $(\mathbf{u}_{back}, p_{back})$ be the solution to the Navier-Stokes equations with the inlet condition "borrowed" from the reference problem and the following boundary conditions on Γ_{wall} and Γ_{out}:

$$(\mu\nabla\mathbf{u}_{back} - p_{back}\mathbf{I})\mathbf{n} = (\mu\nabla\mathbf{u}_{ref} - p_{ref}\mathbf{I})\mathbf{n} \quad \text{on} \quad \Gamma_{in}\times(0,T), \tag{45}$$

$$\mathbf{u}_{back} = \mathbf{0} \quad \text{on} \quad \Gamma_{wall}\times(0,T), \tag{46}$$

$$(\mu\nabla\mathbf{u}_{back} - p_{back}\mathbf{I})\mathbf{n} = \mathbf{0} \quad \text{on} \quad \Gamma_{out}\times(0,T). \tag{47}$$

Hereafter, we call *backflow problem* the Navier-Stokes problem with boundary conditions (45)-(47). Since we prescribe Neumann boundary condition (45) at Γ_{in}, the problem becomes unstable because of the $\mathbf{u}\cdot\mathbf{n}$ term and therefore backflow stabilization at the inflow boundary is needed. To this purpose, we use the EFR scheme for the backflow problem. The numerical results obtained with the EFR algorithm are then compared to the reference solution.

Remark. The reference and the backflow boundary problems are solved with the same mesh, so the boundary data $(\mu\nabla\mathbf{u}_{ref} - p_{ref}\mathbf{I})\mathbf{n}$ on Γ_{in} are promptly retrieved in the finite element formulation at each time step by taking the residual of the system assembled for the reference problem *before the enforcement of the Dirichlet condition* (42). In fact, this residual applied to the reference solution returns at the degrees of freedom of Γ_{in} the vector to be prescribed as boundary data for condition (45) with no additional numerical error.

At each time iteration $n+1$, we perform the following three steps:

1. Solve the reference problem.
2. Compute the residual of the system before the application of the Dirichlet inflow condition (42) to obtain the weak form of the traction to be used as data in (45).
3. Solve the backflow problem stabilized by the EFR scheme.

3.1.2. Numerical results

We approximate the solution of the backflow problem over time interval $[0, 0.5]$ s, with time step $\Delta t = 5\times10^{-3}$ s. The peak backflow occurs at $t = 0.48$ s.

The combination of geometrical and physical parameters described in Sec. 3.1 is similar to the physiological backflow conditions that arise in aortic branches like supra aortic, renal and celiac arteries during the deceleration phase of blood flow. The peak Reynolds number for this test is around 200. The spatial domain is discretized with an unstructured tetrahedral mesh with the minimum mesh size $h_{min} = 0.07$ cm and average mesh size $h_{avg} = 0.12$ cm. The choice of the spatial discretization is such that the reference problem is solved without the need of stabilization for the convective term.

With the EFR-LES model with $\chi = 0.4$ and $\delta = h_{avg}$, we obtain a solution that compares well with the reference solution. The choice of δ is consistent with the general strategies advocated in the literature (δ scaling linearly with the mesh size), while the choice of χ here is empirical, since we have no theoretical background for a specific choice. While the Theorem states that the backflow stabilization becomes effective for $\chi \to 1^-$, we opted for a selection of a smaller χ, to

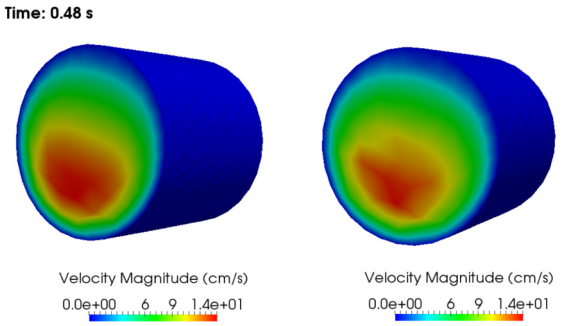

Fig. 2. Test 1: velocity magnitude at the inflow boundary at the time when peak backflow occurs. Left: reference solution. Right: solution to the backflow problem stabilized by EFR scheme.

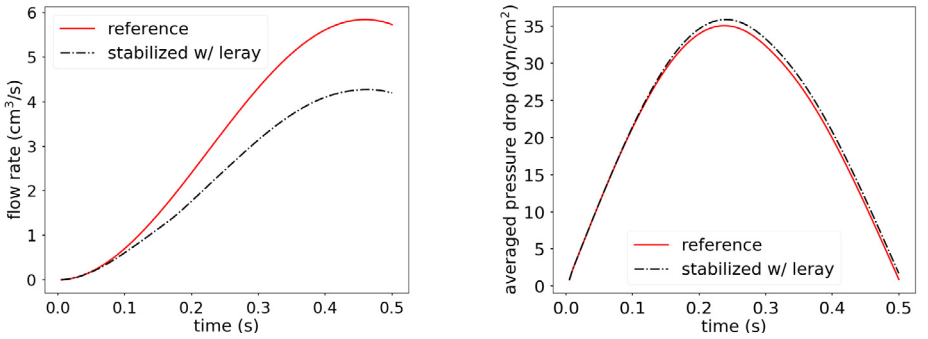

(a) Flow rate at Γ_{in} over time

(b) Pressure drop over time

Fig. 3. Test 1: flow rate at Γ_{in} over time and pressure drop over time - comparison between the reference and the stabilized solutions.

be progressively increased in order to achieve stability. For $\chi = 0.4$, we get a stable result. In particular, we get an accurate pressure drop over time and velocity magnitude at Γ_{in}, as shown in Figs. 2 and 3b, respectively. Notice that Fig. 3b pinpoints the excellent reconstruction of the pressure. Fig. 3a shows flow rate at Γ_{in} over time. We see that the stabilization introduces dissipation. This dissipation, taken as the maximum reduction of the stabilized flow rate vs. the reference solution, is around the 30%. This damping occurs in this specific test and it compares very well with the extensive results presented in [9]. In fact, the flow rate damping induced by popular stabilization techniques in the 2D benchmark of reference [9] can be up to the 90% (see, e.g., Fig. 4 in [9]). These percentages refer to the peak of the dissipation in a specific boundary point. We notice that the damping effect over the entire domain in realistic simulations is much less, as the subsequent numerical simulations will demonstrate. It is enough to get a stable solution and it is worth to mention that there is no boundary condition modification in the approach we propose, since the backflow instability is fixed directly by the LES modeling.

We stress again that success of the EFR-LES model as a backflow stabilization technique depends on the two parameters δ and χ. By carefully tuning these parameters, stable but less damped inflow rates can be achieved. In the absence of theoretical statements, and consistently with the literature in this field (where these parameters are recognized to be generally problem-dependent), the next test aims at establishing some qualitative indications.

3.2. Test 2: reversed flow in a curved channel

For this second benchmark test, an idealized curved tube that can possibly trigger backflow instability is considered. The aim is to investigate the sensitivity of the stabilization to model and discretization parameters in an idealized - yet nontrivial - case and to probe the interplay between these parameters and the discretization.

3.2.1. Problem setup

The idealized geometry under consideration is a portion of a torus whose cross-section has a decreasing radius, from 0.7 cm at one end to 0.3 cm at the other end as in Fig. 4. We consider the flow of an incompressible fluid with the kinematic viscosity $\nu = \frac{\mu}{\rho} = 0.01$ cm^2/s for this problem. Let the section with the largest (resp., smallest) diameter be the inlet (resp., outlet).

Three unstructured tetrahedral meshes were created with *NetGen* [42] (Fig. 4). These meshes have progressive refinements to check that the instability is due to backflows and not to under-refinement. The details about the three different

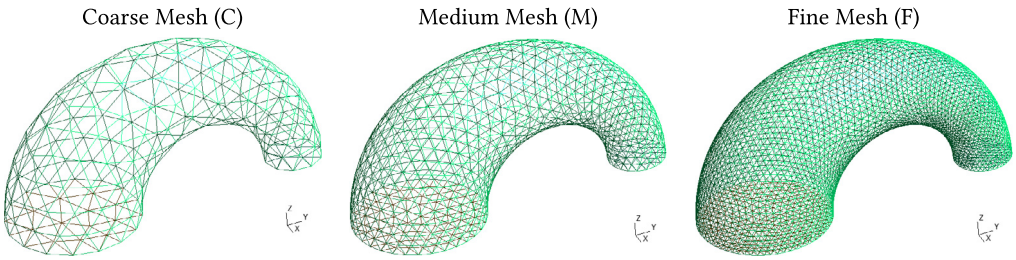

Fig. 4. Test 2: progressively refined meshes for the geometry, visualization of the surface triangles. GMSH [43,44] visualization with green lines in the foreground and black lines in the background. (For interpretation of the colors in the figure(s), the reader is referred to the web version of this article.)

Table 1
Test 2: mesh details for the three meshes under consideration.

Mesh	# nodes	# surface elements	# tetrahedra	h_{min}	h_{max}
C	266	418	824	0.191	0.805
M	1564	1672	6592	0.095	0.591
F	10555	6688	52736	0.047	0.295

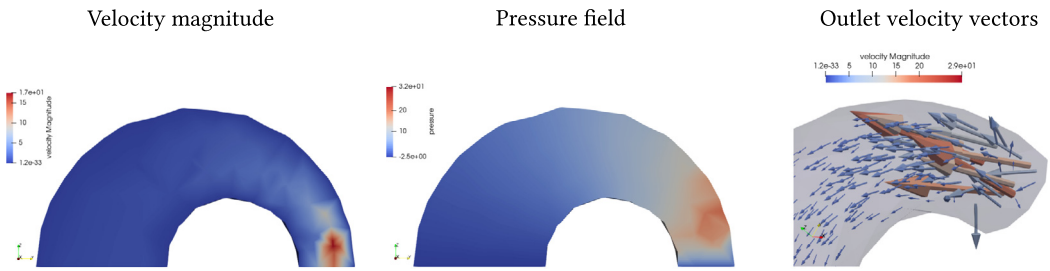

Fig. 5. Test 2: velocity magnitude (left) and pressure field (center) on a section of the domain, and velocity vectors near the outlet (right) at time $t = 1.0$ s computed by the Navier-Stokes solver (no LES modeling) with mesh C and time step $\Delta t = 0.1$ s.

meshes are listed in Table 1. From now on, the three cases will be referred to as *coarse mesh* (C), *medium mesh* (M) and *fine mesh* (F).

3.2.2. Numerical results

We preliminarily run the Navier-Stokes solver (no LES modeling) with the three meshes under consideration to certify that the reason of the instability is due to the backflow. The flow in this case is driven by a periodic pressure drop described by $8\sin(\pi t)$. A no-slip boundary condition is prescribed on the lateral wall. The simulation is started from fluid at rest and has a peak Reynolds number of about 800.

The velocity magnitude and pressure field on the medial plane, and velocity vectors near the outlet at time 1.0 s computed with mesh C are shown in Fig. 5. One can clearly see the onset of the instability near the outlet. The instability occurred for all meshes. In particular, they arise at time $t = 1.0, 0.9, 0.8$ s for mesh C, M and F, respectively. The fact that the instability do not disappear or reduce as the mesh gets refined indicates that the cause is the backflow, rather than the large Reynolds number.

Successively, we focus on meshes M and F with two different time steps, $\Delta t = 0.01$ s and 0.005 s and our EFR-LES scheme. With these time steps and these meshes, the BDF2 semi-implicit time advancing scheme is stable. The ultimate goal is a qualitative understanding of how δ and χ should be selected in practice. The flow in this case is driven by a parabolic inflow (at the larger entrance) with the inflow rate of $2\sin(\pi t)$. The no-slip boundary condition is prescribed on the lateral wall and the homogeneous Neumann condition is enforced at the outlet. The simulation starts at rest and has a peak Reynolds number of about 300.

We tested the statement of the Theorem that for χ large enough backflow instabilities are suppressed. The results for the mesh F and $\Delta t = 0.005$ s, $\delta = h_{min}$ and two different choices of χ, 0.04 and 0.06 respectively, are reported in Fig. 6. As shown in Fig. 6, for $\chi = 0.04$ the simulation suffers from backflow instability, while it runs regularly for $\chi = 0.06$. Therefore, the results confirm that EFR-LES with a large enough χ damps backflow instabilities.

In a subsequent set of simulations, we tested the interplay between χ and δ. The rationale is to verify that they may mutually compensate, so that a large figure for one can reduce the value of the other. The value of the minimal relaxation parameter that attains stability for different values of δ is reported in Table 2. In one case, we selected $\delta = h_{min}$ (as recommended in the relevant literature on EFR-LES), in the other one, we fixed $\delta = 0.9$. The results show that, in general, with a larger δ, χ can be decreased to obtain the stability. For instance, for the mesh F ($\Delta t = 0.01$ s), with $\delta = 0.9$ a relaxation

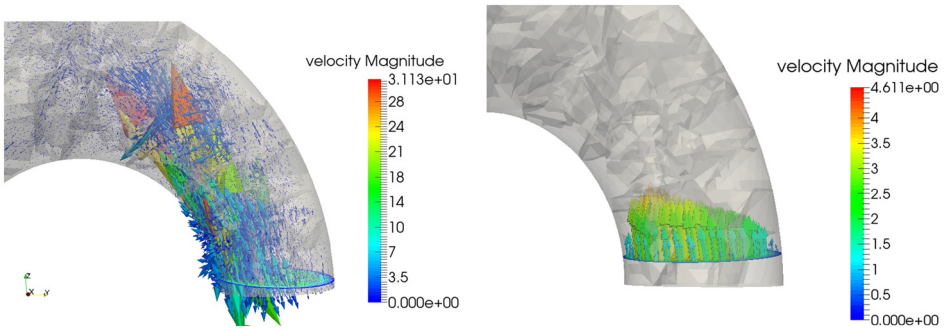

Fig. 6. Test 2: Role of χ for suppressing backflows instability. On mesh F, with $\Delta t = 0.005$ s, for $\delta = h_{min}$, a value of $\chi = 0.04$ does not prevent backflow instability (left), while $\chi = 0.06$ does (right).

Table 2
Test 2: Minimal values of χ to obtain stability for different values of δ. A larger δ can be compensated by a smaller χ (and vice-versa).

$\delta = h_{min}$			
Mesh		M	F
Δt	0.01	0.07	0.08
	0.005	0.04	0.06

$\delta = 0.9$			
Mesh		M	F
Δt	0.01	0.06	0.06
	0.005	0.04	0.05

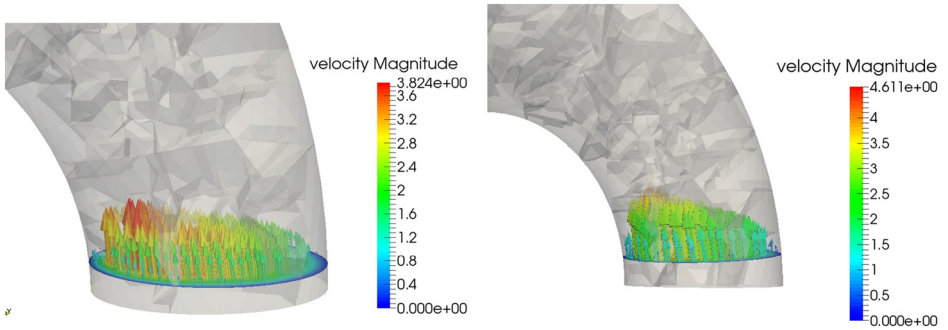

Fig. 7. Test 2: Interplay between χ and Δt for the mesh F. Time step $\Delta t = 0.01$ is stable with $\chi = 0.08$ (left), while for $\Delta t = 0.005$ stability requires $\chi = 0.06$ (right). In the latter case, the solution shows less dissipation - as expected - inferred by the larger velocity magnitude.

of $\chi = 0.06$ is enough for stabilization, while we need at least $\chi = 0.08$ for a smaller δ. On the other hand, without relaxation, a large δ is however not sufficient, i.e. χ must be always large enough ($\chi = 0$ does not work). For the smaller Δt ($\Delta t = 0.005$ s), the value of χ that guarantees stability is virtually independent of δ.

Finally, we tested the interplay between the EFR-LES parameters and the time discretization. It is generally recommended [27] that χ scales with Δt. However, this recommendation refers to the modeling of turbulence and not to the backflow stabilization. It can be inferred from Table 2 that the reduction of the relaxation parameter with Δt is apparent, yet the scaling is sub-linear. This holds for the two meshes M and F when $\delta = h_{min}$.

We qualitatively corroborate this statement with Fig. 7, where we show the results on the fine mesh, with two different time steps. With a smaller time step we can reduce the relaxation parameter and the results - although comparable - show less numerical dissipation.

It has been pointed out that the optimal choice of the parameters in EFR-LES is generally problem-dependent [45]. In absence of a precise theoretical framework, these tests will lead to our conclusive statements about the practical selection of those parameters (see Sec. 4).

3.3. Test 3: hemodynamics in a patient-specific aorta with patient-specific inflow data

After testing the backflow stabilization performance of the EFR-LES model in idealized geometries, we consider a complicated geometry used for a real clinical study: a patient-specific aorta with an abdominal aneurysm. In this geometry, the hemodynamics driven by the patient-specific inflow rate at the ascending aorta suffers from the backflow instability.

(a) geo1 (without flow extension)

(b) geo2 (with flow extension)

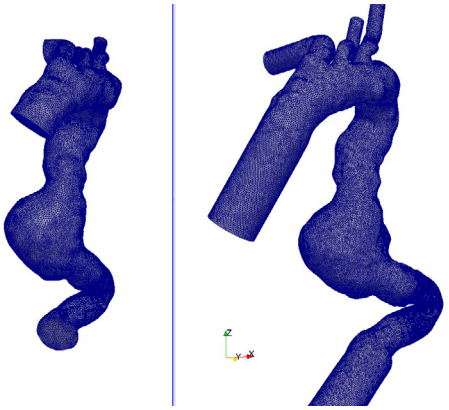

(c) meshes for geo1 and geo2

Fig. 8. Test 3: patient-specific aorta with abdominal aneurysm reconstructed from CT images (a) without flow extensions (geometry geo1); (b) with flow extensions (geometry geo2); (c) a visualization of the spatial discretization of geo1 (left) and geo2 (right).

3.3.1. Problem setup

The patient's aorta is reconstructed from the CT images using VMTK (Vascular Modeling Tool Kit) [46]. The data were collected in the frame of the iCardioCloud Project [47,7]. The supra-aortic branches, i.e. the brachiocephalic, left common carotid and left subclavian arteries, are included in the image reconstruction, shown as the geometry geo1 in Fig. 8a. A second geometry, called geo2 (see Fig. 8b), was then created by adding artificial flow extensions to all the boundaries of geo1. The extensions, assembled with VMTK, are cylinders with axis along the tangent to the centerline at the original boundaries.

The patient-specific inflow rate shown in Fig. 9 with a parabolic velocity profile is imposed as the inflow boundary condition at the ascending aorta. The assumption on the velocity profile is common practice due to the lack of the pointwise velocity data. The resulting Reynolds number at peak systole at the ascending aorta is $Re = 4659$.

At the outflow boundaries Γ_i, for $i = 1, 2, 3, 4$, we prescribe a set of boundary conditions quite popular in the computational hemodynamics community. These conditions stem from a surrogate modeling of the peripheral circulation that goes under the name of Three-Element Windkessel (3WK) [2,4,7]. In short, the peripheral circulation is described by a differential equation in time that combines the outflow average pressure $\bar{p} \equiv \int_{\Gamma_i} p d\gamma / \int_{\Gamma_i} d\gamma$ and the flow rate $Q \equiv \rho \int_{\Gamma_i} \mathbf{u} \cdot \mathbf{n} d\gamma$. The equation depends on three parameters: R_p and R_d, which represent the viscous dissipation in the proximal and distal region of the outflow, and C (called compliance), which denotes the deformation of the arteries. Then, the three-element Windkessel condition at each outflow Γ_i reads

$$p\mathbf{n}_i - 2\mu\nabla^s\mathbf{u} \cdot \mathbf{n}_i = g_i\mathbf{n}_i$$

with $g_i = g_i(t)$ function (with the dimension of a pressure) of time only:

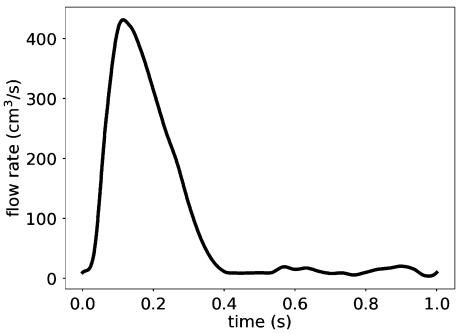

Fig. 9. Test 3: patient-specific inflow rate over a cardiac cycle.

Table 3
Test 3: patient-specific Windkessel parameters.

Aortic branches	Three-element Windkessel parameters		
	R_p 10^3 dyn s/cm^5	R_d 10^4 dyn s/cm^5	C 10^{-4} cm^5/dyn
Brachiocephalic artery	0.78	2.03	0.93
Left common carotid	3.80	4.50	0.34
Left subclavian	1.39	3.20	0.58
Abdominal aortic outlet	0.13	0.15	10.90

Table 4
Test 3: details of the meshes used for geometries `geo1` and `geo2`.

Geometry	No. of nodes	h_{min}	h_{avg}
`geo1`	817k	0.03 cm	0.16 cm
`geo2`	4657k	0.04 cm	0.13 cm

$$g_i(t) = g_i(0)e^{-t/(CR_d)} + R_p\left(Q(t) - Q(0)e^{-t/(CR_d)}\right) + \frac{1}{C}\left(\int_0^t Q(\tau)e^{-(t-\tau)/CR_d}d\tau\right). \tag{48}$$

Notice that Q is unknown as it depends on the velocity. These conditions have the same functional form as the conditions (31), advocated to stabilize the backflows. However, here the parameters are not tuned to control the negative energy term, rather to provide a lumped parameter description of the downstream circulation. There is no guarantee, in general, that these values stabilize the backflows, as we will see in the results. The parameters of the 3WK model we use are listed in Table 3 and are determined for each outflow using available patient's data as described in [7]. A homogeneous Dirichlet condition is imposed on the arterial wall.

Geometries `geo1` and `geo2` are discretized with unstructured tetrahedra, as shown in Fig. 8c. The details of the meshes are reported in Table 4. Notice that refinement level for the two meshes is comparable. However, due to the presence of the flow extensions in `geo2`, the number of degrees of freedom for the corresponding mesh is larger.

We conducted three numerical tests, called *test 3a, 3b* and *3c*. For all the simulations, we set $\Delta t = 5 \times 10^{-3}$ s and $T = 6$ s, which corresponds to 6 cardiac cycles. The specific setup of the tests is reported in Table 5. *Test 3a* uses `geo1` and no backflow stabilization at the Neumann boundaries to demonstrate the existence of backflow instability in this patient-specific case. *Test 3b* checks that the backflow instability in `geo1` is suppressed when using the EFR-LES model with $\chi = 0.9$ and $\delta = h_{min}$. The boundary conditions for the EFR-LES model are given by:

$$\begin{aligned}
\mathbf{v}^{n+1} = \mathbf{v}_f^{n+1} = \mathbf{u}_{in}^{n+1} \quad &\text{on} \quad \Gamma_{in},\\
\mathbf{v}^{n+1} = \mathbf{v}_f^{n+1} = \mathbf{0} \quad &\text{on} \quad \Gamma_{wall},\\
(\mu\nabla\mathbf{v}^{n+1} - q^{n+1}\mathbf{I})\mathbf{n}_i = g_i\mathbf{n}_i \quad &\text{on} \quad \Gamma_i,\\
(\mu_f^{n+1}\nabla\mathbf{v}_f^{n+1} - q_f^{n+1}\mathbf{I})\mathbf{n}_i = \mathbf{0} \quad &\text{on} \quad \Gamma_i,
\end{aligned}$$

where the g_i, for $i = 1, 2, 3, 4$, are obtained from the Windkessel model at the outflow boundaries Γ_i as specified in (48). In order further evaluate the performance of the EFR-LES model, we designed *Test 3c* which features a solution comparable to the solution of *Test 3b* but obtained with a different method. For *Test 3c*, we use `geo2`. The flow extensions in `geo2` are supposed to introduce an energy dissipation that empirically mitigates the impact of backflows [7]. Finally, we recall that

Table 5
Test 3: setup for the three tests concerning the patient-specific geometry.

Setup	Test		
	Test 3a	*Test 3b*	*Test 3c*
Geometry	`geo1`	`geo1`	`geo2`
EFR-LES model		√	
Streamline diffusion	√		√
Velocity gradient based backflow stabilization			√
Numerically stable	No	Yes	Yes

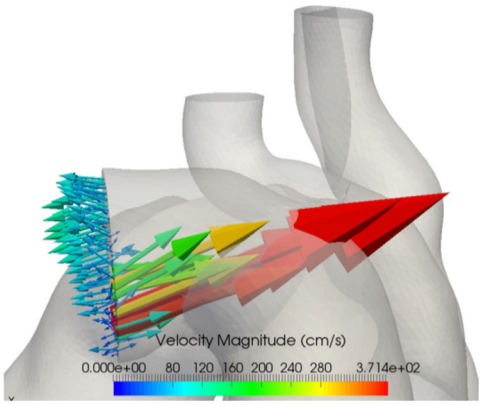

Fig. 10. Test 3a: velocity vectors at the brachiocephalic artery at $t = 0.32$ s, shortly before the simulation crashes.

the EFR-LES model in *Test 3b* takes care of the instability due the convective term too. To overcome such instability in *Test 3a* and *3c*, we apply the classical streamline diffusion stabilization.

The results for *Test 3b* and *3c* presented in the following subsection refer to the last cardiac cycle.

3.3.2. Numerical results

During the deceleration period following the peak systole, the flow is reverted at the brachiocephalic and left subclavian arteries. The backflow at these two branches causes the instability for *Test 3a* and eventually makes the simulation crash. Therefore, backflow stabilization is necessary in order to obtain stable numerical results for this patient-specific case. The unstable velocity at the brachiocephalic artery occurring at $t = 0.32$ s is shown in Fig. 10. *Test 3b* is numerically stable, indicating that the EFR-LES model successfully suppresses the backflow instability. *Test 3c* is numerically stable too.

We compare the results of *Test 3b* and *3c*. The comparison of flow rate and average pressure at each outflow boundary (at the same locations) over time is shown in Figs. 11 and 12, respectively. First of all, from Fig. 11 we observe that the results from both *Test 3b* and *3c* capture the reverse flow at the brachiocephalic and left subclavian arteries at the end of systole. The two computed flow rates from *Test 3b and 3c* are consistent, following similar dynamics. The pressure at the supra-aortic branches of *Test 3b* is higher than *Test 3c*. Apart from these details, they follow similar dynamics. The flows rates from *Test 3b and 3c* are more in agreement than the pressures.

In Figs. 13 and 14, we report the velocity magnitude and vectors from *Test 3b* and *3c* at the brachiocephalic branch at time $t = 0.32$ s, which corresponds to the peak backflow. The stabilized velocity from both tests are qualitatively consistent, however their absolute magnitudes are not the same. We argue that the velocity magnitude in *Test 3c* is smaller due to the artificial diffusion introduced by the streamline diffusion stabilization. In Fig. 15, the velocity vectors at the same branch are compared at time $t = 0.13$ s, which corresponds to the peak forward flow. We observe that the velocity field at the brachiocephalic outflow is more uniform in *Test 3c* than expected in physiological conditions [48–50]. In fact, a physiological flow condition resembles flow in a curved pipe where secondary flow happens [51,52] depending on different Dean numbers. The more uniform velocity is most likely an effect of the penalization on the velocity gradient introduced at the boundary.

The time averaged wall shear stress (TAWSS) is one of the clinical quantities of interest in understanding disease progression of abdominal aneurysm [53]. In Fig. 16, we compare the TAWSS computed from *Test 3b* and *Test 3c*. The distributions of the magnitude of TAWSS agree well qualitatively, in particular at the location of interest, i.e. the abdominal aneurysm. However, higher TAWSS is observed at the supra-aortic branches in *Test 3b*, which agrees with physiological conditions [54, 55].

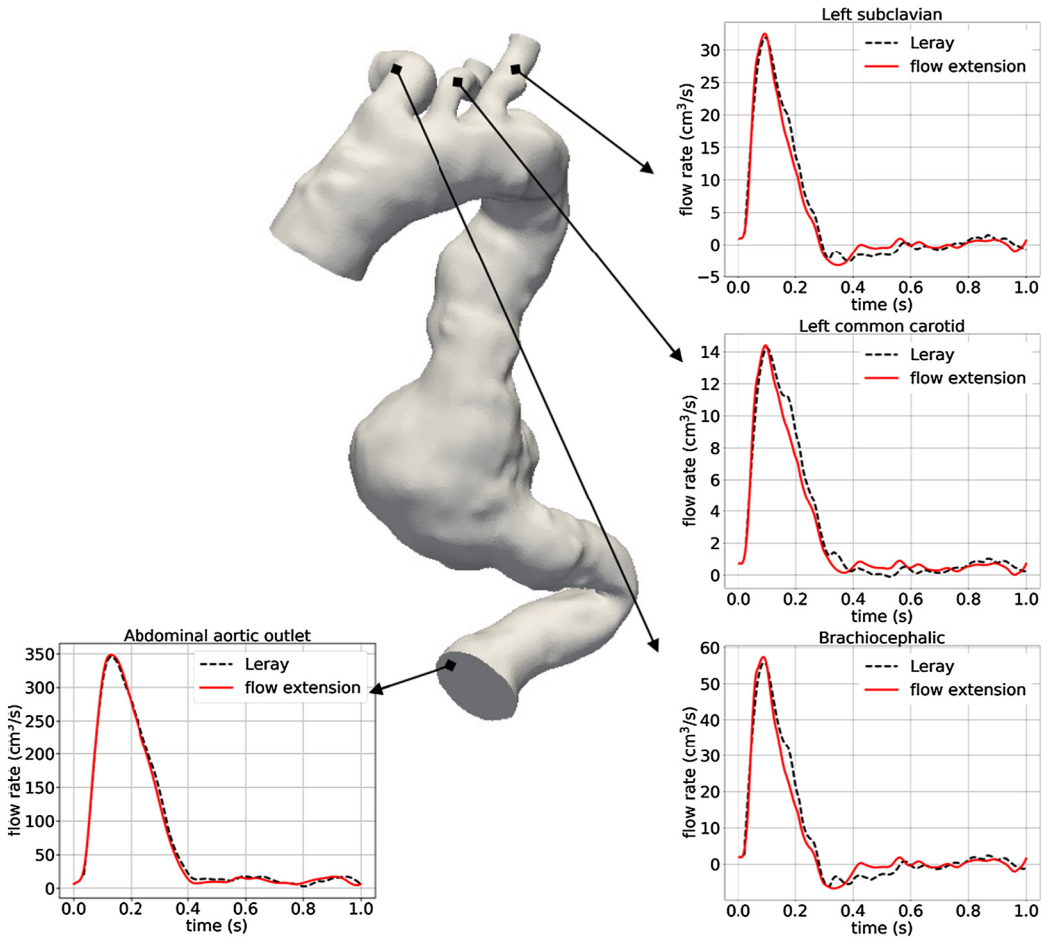

Fig. 11. Test 3b (Leray) and 3c (flow extension): comparison of the computed flow rate at each outflow boundary over time.

4. Discussion and conclusion

This work originates from a long-term experience in computational hemodynamics, applied to patient-specific settings. The gap between theory and practice in this context [4] challenges both accuracy and efficiency of numerical tools used for the clinical practice. One of the most problematic aspects is the boundary conditions.

The access to data to use for boundary conditions is prevented by practical and ethical issues, while there is abundance of images to reconstruct the morphology (the so called *"image-legacy" problem*). This leads to the introduction of simplified models to retrieve boundary data (see, e.g., [7]) without impairing the reliability of the simulations. On the other hand, homogeneous Neumann conditions, i.e., "do-nothing" conditions [1], are typically set in the absence of alternatives. This is due to the fact that Neumann conditions are generally less invasive on the numerical solution, being "natural" to a given differential problem (in its variational form). This has some drawbacks, particularly for the stability of the physical problem and its numerical consequences. The flow reversals occurring in some vascular districts, like the aorta, call for stable solvers.

Stability can be achieved by modifying the domain of interest, with the introduction of the so called *flow extensions*, that damp the incoming energy carried in by the flow. This solution - used also for flow rate conditions at the inflow to prescribe the arbitrary velocity profile far away from the region of interest - is highly empirical and, in spite of its relative conceptual simplicity, requires the construction of alterations of the domain of interest that are not always easy [56]. Artifacts may be introduced by an imperfect alignment of the extensions with the centerline of the region of interest. In any case, flow extensions require additional degrees of freedom in the computation, inducing an extra computational cost. For instance, in our numerical experiment *Test 3b*, the CPU time per time step is about 30% of the CPU time per time step required by *Test 3c* with the same computational power (4 cores, i.e. 192 nodes, on the Extreme Science and Engineering Discovery Environment stampede2 [57]), due to the extra DOFs introduced by the flow extensions.

Another way for damping the incoming energy is the use of Robin conditions [14,31], which is conceptually similar to the flow extension, but with no additional computational effort. It is worth noting that Robin-like conditions (advocated also for the well posedness of geometrical multiscale models [58]) for Navier-Stokes problems are not standard and may

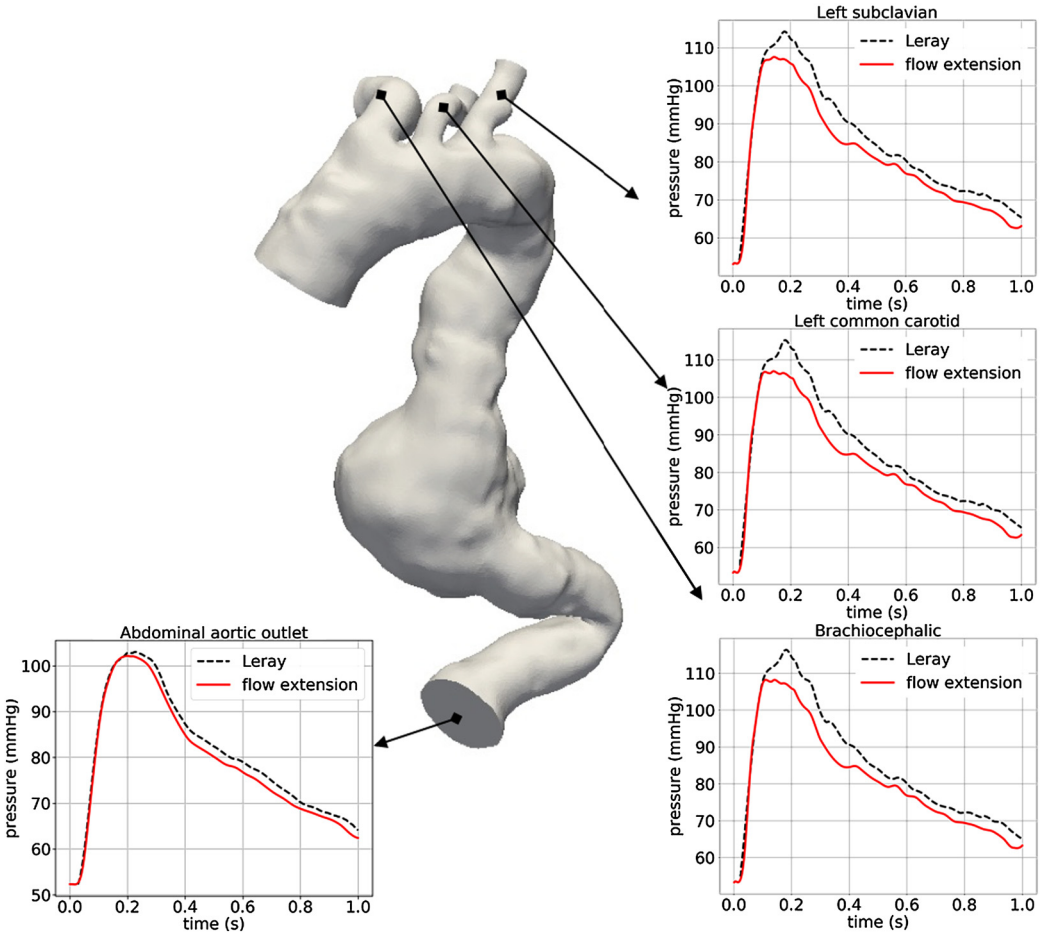

Fig. 12. Test 3b (Leray) and 3c (flow extension): comparison of the average pressure at each outflow boundary over time.

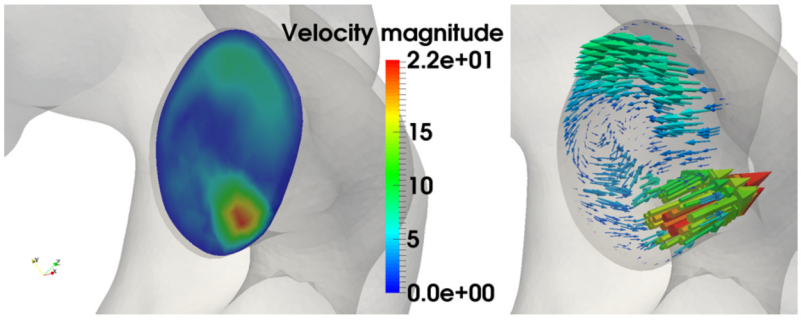

Fig. 13. Test 3b: velocity magnitude (left) and velocity vectors (right) at the brachiocephalic branch at $t = 0.32$ s, which corresponds to the peak backflow.

require specific coding; moreover, the fine tuning of the resistance needs physical and/or numerical arguments. Other more sophisticated approaches have been considered in [9,11–13,30].

This paper stems from the practical observation that adding a specific modeling of unresolved scales like the Leray-Deconvolution approach formulated according to the EFR scheme in aortic simulations rarely suffered from the instability due to the flow reversal. While the aortic flow (Reynolds number of the order of few thousands) is amenable to direct numerical simulations, the large volume of clinical data we are considering [6,7] suggests the introduction of an efficient modeling at relatively coarse mesh discretizations, while guaranteeing a level of accuracy relevant to the clinical practice. From this perspective, LES modeling provides an excellent trade-off between accuracy and efficiency required by patient-specific settings in computer-aided clinical trials. With this motivation, we discovered that our LES modeling may control any backflows and in this paper we provide a rigorous proof and extensive numerical evidence. While not all the simulations in computational hemodynamics suffer from flow reversal, aorta is one of the districts interested by this phenomenon. In

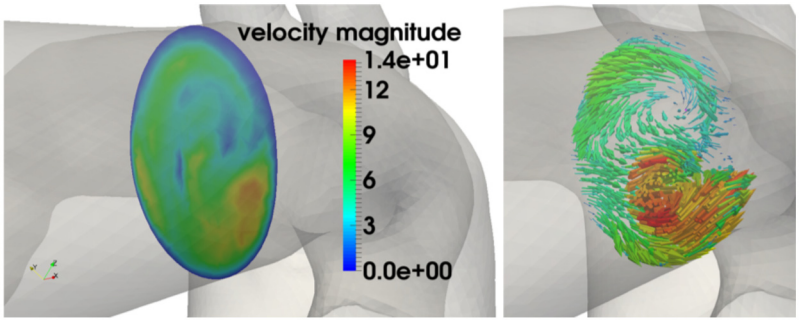

Fig. 14. Test 3c: velocity magnitude (left) and velocity vectors (right) at the brachiocephalic branch at $t = 0.32$ s, which corresponds to the peak backflow.

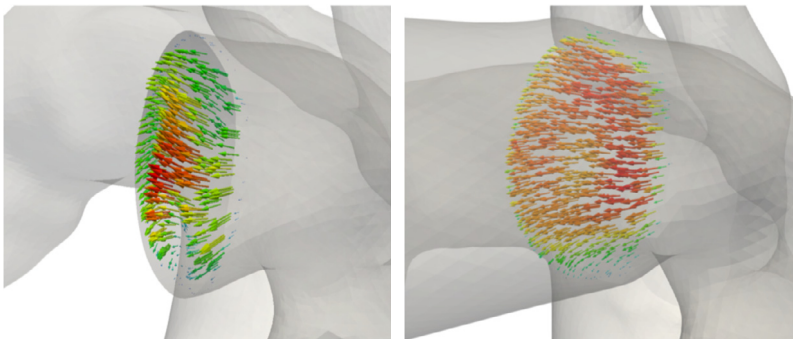

(a) *Test 3b* (b) *Test 3c*

Fig. 15. Test 3b and 3c: velocity vectors at the brachiocephalic branch at $t = 0.13$ s, which corresponds to the peak forward flow. The color scales are the same in the two pictures.

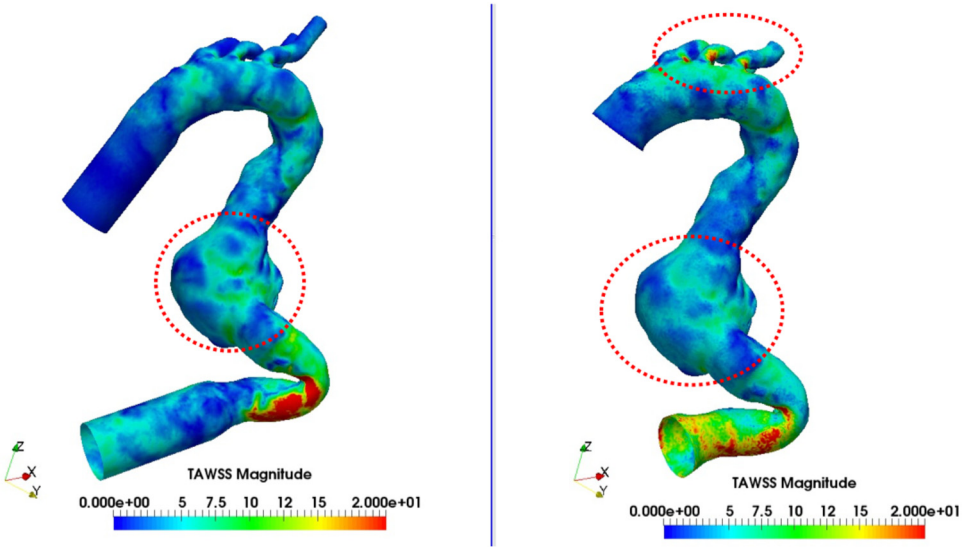

Fig. 16. Test 3c and 3b: comparison of the TAWSS for *Test 3c* (left) and *Test 3b* (right).

favor of our LES approach, we prove here this serendipity circumstance that fixes the need of modeling unresolved scales and the backflow instability at once ("two birds with one stone").

On the choice of the stabilization parameters. Our Theorem is based on energy considerations and a continuity argument with respect to the parameters, particularly the relaxation parameter χ. Unfortunately, our proof does not give specific recipes for calibrating model parameters χ and δ. This attains to an extensive sensitivity analysis of the role of χ and δ that is a work in progress [45,59]. In [45], the sensitivity analysis on δ (therein called α) suggests that the velocity computed by our scheme

does actually depend on δ in a nonuniform problem-dependent way, so that the selection of the radius may be based on the mesh size in a conservative sense, possibly corrected by some adaptive strategies. In [59], the interplay between the radius and other possible data affecting the results is investigated using Polynomial Chaos Expansion based Sobol' Indexes, specifically for hemodynamics problems. The results show that the choice of δ has an impact only in some specific parts of the heart beat (the diastolic phase) and, in any case, is definitely less impactful than the geometry of the computational domain. These analyses pinpoint the need for further investigations, that are expected to be largely problem-dependent.

Our results empirically led us to some practical guidelines:

1. Selecting δ proportional to h_{min} is generally a recommended strategy, possibly to be corrected in an adaptive fashion with the solution of a sensitivity problem as suggested in [45] and in particular during the phases of the simulation (like, e.g., during the diastole) when the solution is significantly affected by the filter radius (as noted in [59]).
2. It is argued for the turbulence modeling that χ should be proportional to Δt. However, suppression of backflow instability is not related to the time-discretization, so the combination of the stabilizing effects calls for a sub-linear dependence on the time step.
3. Generally, a small filter radius (for instance for a fine mesh) calls for a larger relaxation parameter (and vice-versa). However, backflow stabilization requires some relaxation ($\chi > 0$) even for a large radius δ.

Setting up adaptive strategies will be subject of future developments. As a rule-of-thumb, in our next applications of this solver for aortic simulations (following up [6]) we plan to select $\delta = h_{min}$ and to adjust manually or adaptively χ to prevent instabilities, starting from a tentative value of $\chi \approx f\Delta t$, where f is a problem-dependent factor.

Declaration of competing interest

The authors declare that they have no known competing financial interests or personal relationships that could have appeared to influence the work reported in this paper.

Acknowledgements

Simulations in this study were carried out on the Extreme Science and Engineering Discovery Environment (XSEDE), which is supported by National Science Foundation grant number TG-ASC160069. H. Xu, A. Quaini and A. Veneziani acknowledge the support of the US National Science Foundation collaborative project NSF-DMS 1620406/1620384. F. Di Massimo acknowledges the Department of Mathematics of Emory University for the productive and friendly environment offered during her visit in Fall 2018. The support of the Fondazione Cariplo for the iCardioCloud Project 2013-1779 is gratefully acknowledged for the patient-specific images. In particular, the support of Ferdinando Auricchio from the Department of Civil Engineering and Architecture at the University of Pavia, Italy and Rodrigo Romarowski from IRCCS Policlinico San Donato, Milan, Italy for the imaging processing of the patient-specific case is warmly acknowledged.

References

[1] J.G. Heywood, R. Rannacher, S. Turek, Artificial boundaries and flux and pressure conditions for the incompressible Navier–Stokes equations, Int. J. Numer. Methods Fluids 22 (5) (1996) 325–352.
[2] L. Formaggia, A. Quarteroni, A. Veneziani, Cardiovascular Mathematics: Modeling and Simulation of the Circulatory System, vol. 1, Springer Science & Business Media, 2010.
[3] U. Morbiducci, R. Ponzini, D. Gallo, C. Bignardi, G. Rizzo, Inflow boundary conditions for image-based computational hemodynamics: impact of idealized versus measured velocity profiles in the human aorta, J. Biomech. 46 (1) (2013) 102–109.
[4] A. Quarteroni, A. Veneziani, C. Vergara, Geometric multiscale modeling of the cardiovascular system, between theory and practice, Comput. Methods Appl. Mech. Eng. 302 (2016) 193–252.
[5] A. Veneziani, C. Vergara, Flow rate defective boundary conditions in haemodynamics simulations, Int. J. Numer. Methods Fluids 47 (8–9) (2005) 803–816.
[6] H. Xu, M. Piccinelli, B.G. Leshnower, A. Lefieux, W.R. Taylor, A. Veneziani, Coupled morphological–hemodynamic computational analysis of type b aortic dissection: a longitudinal study, Ann. Biomed. Eng. 46 (7) (2018) 927–939.
[7] R.M. Romarowski, A. Lefieux, S. Morganti, A. Veneziani, F. Auricchio, Patient-specific CFD modelling in the thoracic aorta with PC-MRI-based boundary conditions: a least-square three-element Windkessel approach, Int. J. Numer. Methods Biomed. Eng. 34 (11) (2018) e3134.
[8] I.E. Vignon-Clementel, C.A. Figueroa, K.E. Jansen, C.A. Taylor, Outflow boundary conditions for three-dimensional finite element modeling of blood flow and pressure in arteries, Comput. Methods Appl. Mech. Eng. 195 (29) (2006) 3776–3796.
[9] C. Bertoglio, A. Caiazzo, Y. Bazilevs, M. Braack, M. Esmaily, V. Gravemeier, A.L. Marsden, O. Pironneau, I.E. Vignon-Clementel, W.A. Wall, Benchmark problems for numerical treatment of backflow at open boundaries, Int. J. Numer. Methods Biomed. Eng. 34 (2) (2018) e2918.
[10] G. Arbia, I. Vignon-Clementel, T.-Y. Hsia, J.-F. Gerbeau, M. of Congenital Hearts Alliance (MOCHA) Investigators, et al., Modified Navier–Stokes equations for the outflow boundary conditions in hemodynamics, Eur. J. Mech. B, Fluids 60 (2016) 175–188.
[11] C. Bertoglio, A. Caiazzo, A Stokes-residual backflow stabilization method applied to physiological flows, J. Comput. Phys. 313 (2016) 260–278.
[12] C. Bertoglio, A. Caiazzo, A tangential regularization method for backflow stabilization in hemodynamics, J. Comput. Phys. 261 (2014) 162–171.
[13] M.E. Moghadam, Y. Bazilevs, T.-Y. Hsia, I.E. Vignon-Clementel, A.L. Marsden, et al., A comparison of outlet boundary treatments for prevention of backflow divergence with relevance to blood flow simulations, Comput. Mech. 48 (3) (2011) 277–291.
[14] C.-H. Bruneau, P. Fabrie, Effective downstream boundary conditions for incompressible Navier–Stokes equations, Int. J. Numer. Methods Fluids 19 (8) (1994) 693–705.

[15] J. Lantz, T. Ebbers, J. Engvall, M. Karlsson, Numerical and experimental assessment of turbulent kinetic energy in an aortic coarctation, J. Biomech. 46 (11) (2013) 1851–1858.
[16] H. Ha, M. Ziegler, M. Welander, N. Bjarnegård, C.-J. Carlhäll, M. Lindenberger, T. Länne, T. Ebbers, P. Dyverfeldt, Age-related vascular changes affect turbulence in aortic blood flow, Front. Physiol. 9 (2018) 36.
[17] L. Bertagna, A. Quaini, A. Veneziani, Deconvolution-based nonlinear filtering for incompressible flows at moderately large Reynolds numbers, Int. J. Numer. Methods Fluids 81 (8) (2016) 463–488.
[18] J.E. Marsden, T.J. Hughes, Mathematical Foundations of Elasticity, Courier Corporation, 1994.
[19] A.N. Kolmogorov, Dissipation of energy in locally isotropic turbulence, Dokl. Akad. Nauk SSSR 32 (1941) 16.
[20] J. Smagorinsky, General circulation experiments with the primitive equations: I. The basic experiment, Mon. Weather Rev. 91 (3) (1963) 99–164.
[21] B.J. Geurts, D.D. Holm, Leray and LANS-α modelling of turbulent mixing, J. Turbul. 7 (2006) N10.
[22] Y. Bazilevs, V. Calo, J. Cottrell, T. Hughes, A. Reali, G. Scovazzi, Variational multiscale residual-based turbulence modeling for large eddy simulation of incompressible flows, Comput. Methods Appl. Mech. Eng. 197 (1–4) (2007) 173–201.
[23] P. Sagaut, Large Eddy Simulation for Incompressible Flows: An Introduction, Springer Science & Business Media, 2006.
[24] W. Layton, C.C. Manica, M. Neda, L.G. Rebholz, Numerical analysis and computational testing of a high accuracy Leray-deconvolution model of turbulence, Numer. Methods Partial Differ. Equ. 24 (2) (2008) 555–582.
[25] W. Layton, R. Lewandowski, A high accuracy Leray-deconvolution model of turbulence and its limiting behavior, Anal. Appl. 6 (01) (2008) 23–49.
[26] W.J. Layton, L.G. Rebholz, Approximate Deconvolution Models of Turbulence: Analysis, Phenomenology and Numerical Analysis, vol. 2042, Springer Science & Business Media, 2012.
[27] W. Layton, L.G. Rebholz, C. Trenchea, Modular nonlinear filter stabilization of methods for higher Reynolds numbers flow, J. Math. Fluid Mech. 14 (2) (2012) 325–354.
[28] A.L. Bowers, L.G. Rebholz, Numerical study of a regularization model for incompressible flow with deconvolution-based adaptive nonlinear filtering, Comput. Methods Appl. Mech. Eng. 258 (2013) 1–12.
[29] A. Quarteroni, R. Sacco, F. Saleri, Numerical Mathematics, vol. 37, Springer Science & Business Media, 2010.
[30] H.J. Kim, C. Figueroa, T. Hughes, K. Jansen, C. Taylor, Augmented Lagrangian method for constraining the shape of velocity profiles at outlet boundaries for three-dimensional finite element simulations of blood flow, Comput. Methods Appl. Mech. Eng. 198 (45) (2009) 3551–3566.
[31] C.-H. Bruneau, P. Fabrie, New efficient boundary conditions for incompressible Navier-Stokes equations: a well-posedness result, ESAIM: Math. Model. Numer. Anal. 30 (7) (1996) 815–840.
[32] R. Temam, Navier-Stokes Equations and Nonlinear Functional Analysis, second edition, CBMS-NSF Regional Conference Series in Applied Mathematics, Society for Industrial and Applied Mathematics, 1995.
[33] J.G. Heywood, R. Rannacher, Finite element approximation of the nonstationary Navier-Stokes problem. I. Regularity of solutions and second-order error estimates for spatial discretization, SIAM J. Numer. Anal. 19 (2) (1982) 275–311.
[34] J.G. Heywood, R. Rannacher, Finite element approximation of the nonstationary Navier-Stokes problem. II. Stability of solutions and error estimates uniform in time, SIAM J. Numer. Anal. 23 (4) (1986) 750–777.
[35] J.G. Heywood, R. Rannacher, Finite element approximation of the nonstationary Navier-Stokes problem. III. Smoothing property and higher order error estimates for spatial discretization, SIAM J. Numer. Anal. 25 (3) (1988) 489–512.
[36] J.G. Heywood, R. Rannacher, Finite-element approximation of the nonstationary Navier-Stokes problem. Part IV: Error analysis for second-order time discretization, SIAM J. Numer. Anal. 27 (2) (1990) 353–384.
[37] LifeV parallel finite element library, https://bitbucket.org/lifev-dev/lifev-release/wiki/Home/.
[38] T. Passerini, A. Quaini, U. Villa, A. Veneziani, S. Canic, Validation of an open source framework for the simulation of blood flow in rigid and deformable vessels, Int. J. Numer. Methods Biomed. Eng. 29 (11) (2013) 1192–1213.
[39] F. Hecht, O. Pironneau, A. Le Hyaric, K. Ohtsuka, FreeFem++ Manual, 2005.
[40] J.R. Womersley, Method for the calculation of velocity, rate of flow and viscous drag in arteries when the pressure gradient is known, J. Physiol. 127 (3) (1955) 553–563.
[41] L. Formaggia, F. Saleri, A. Veneziani, Solving Numerical PDEs: Problems, Applications, Exercises, Springer Science & Business Media, 2012.
[42] J. Schöberl, NETGEN: an advancing front 2D/3D-mesh generator based on abstract rules, Comput. Vis. Sci. 1 (1) (1997) 41–52.
[43] C. Geuzaine, J.-F. Remacle, GMSH: a 3-D finite element mesh generator with built-in pre- and post-processing facilities, Int. J. Numer. Methods Eng. 79 (2009) 1309–1331.
[44] The GMSH website, http://gmsh.info/.
[45] L. Bertagna, A. Quaini, L.G. Rebholz, A. Veneziani, On the sensitivity to the filtering radius in Leray models of incompressible flow, in: Contributions to Partial Differential Equations and Applications, Springer, 2019, pp. 111–130.
[46] The Vascular Modeling Toolkit website, http://www.vmtk.org/.
[47] F. Auricchio, M. Conti, A. Lefieux, S. Morganti, A. Reali, F. Sardanelli, F. Secchi, S. Trimarchi, A. Veneziani, Patient-specific analysis of post-operative aortic hemodynamics: a focus on thoracic endovascular repair (TEVAR), Comput. Mech. 54 (4) (2014) 943–953.
[48] S. Gupta, A.R. Popescu, R. De Freitas, D. Thakrar, J. Puthumana, J. Carr, M. Markl, Four-dimensional magnetic resonance flow analysis clarifies paradoxical symptoms in a patient with aortic bypass and retrograde flow mimicking subclavian steal, Circulation 125 (6) (2012) e347–e349.
[49] Y. Amano, R. Takagi, Y. Suzuki, T. Sekine, S. Kumita, M. van Cauteren, Three-dimensional velocity mapping of thoracic aorta and supra-aortic arteries in Takayasu arteritis, J. Magn. Reson. Imaging 31 (6) (2010) 1481–1485.
[50] P. Vasava, P. Jalali, M. Dabagh, P.J. Kolari, Finite element modelling of pulsatile blood flow in idealized model of human aortic arch: study of hypotension and hypertension, Comput. Math. Methods Med. (2012).
[51] L. Talbot, K. Gong, Pulsatile entrance flow in a curved pipe, J. Fluid Mech. 127 (1983) 1–25.
[52] F.T. Smith, Fluid flow into a curved pipe, Proc. R. Soc. Lond. Ser. A, Math. Phys. Sci. 351 (1664) (1976) 71–87.
[53] A.-V. Salsac, S. Sparks, J.-M. Chomaz, J. Lasheras, Evolution of the wall shear stresses during the progressive enlargement of symmetric abdominal aortic aneurysms, J. Fluid Mech. 560 (2006) 19–51.
[54] A. Boccadifuoco, A. Mariotti, K. Capellini, S. Celi, M.V. Salvetti, Validation of numerical simulations of thoracic aorta hemodynamics: comparison with in vivo measurements and stochastic sensitivity analysis, Cardiovasc. Eng. Techn. 9 (4) (2018) 688–706.
[55] L. Ellwein, M.M. Samyn, M. Danduran, S. Schindler-Ivens, S. Liebham, J.F. LaDisa, Toward translating near-infrared spectroscopy oxygen saturation data for the non-invasive prediction of spatial and temporal hemodynamics during exercise, Biomech. Model. Mechanobiol. 16 (1) (2017) 75–96.
[56] L. Antiga, M. Piccinelli, L. Botti, B. Ene-Iordache, A. Remuzzi, D.A. Steinman, An image-based modeling framework for patient-specific computational hemodynamics, Med. Biol. Eng. Comput. 46 (11) (2008) 1097–1112.
[57] J. Towns, T. Cockerill, M. Dahan, I. Foster, K. Gaither, A. Grimshaw, V. Hazlewood, S. Lathrop, D. Lifka, G.D. Peterson, et al., XSEDE: accelerating scientific discovery, Comput. Sci. Eng. 16 (5) (2014) 62–74.
[58] A. Quarteroni, A. Veneziani, Analysis of a geometrical multiscale model based on the coupling of ODE and PDE for blood flow simulations, Multiscale Model. Simul. 1 (2) (2003) 173–195.
[59] H. Xu, D. Baroli, A. Veneziani, Global sensitivity analysis of the nonlinear Leray model using the polynomial chaos expansion based Sobol' indices (in preparation).